# Hemivariational continuum approach for granular solids with damage-induced anisotropy evolution

Dmitry Timofeev (1), Emilio Barchiesi (1), Anil Misra (2), Luca Placidi (3)

October 6, 2020

- (1) International Research Center on Mathematics and Mechanics of Complex Systems (M&MoCS). Università degli Studi dell'Aquila. Via Giovanni Gronchi 18 Zona industriale di Pile 67100, L'Aquila (Italy).
- (2) The University of Kansas. Civil, Environmental and Architectural Engineering Department. 1530 W. 15th Street, Lawrence, KS 66045-7609.
- (3) International Telematic University UNINETTUNO. Faculty of Engineering. Corso Vittorio Emanuele II 39 00186, Roma (Italy). Corresponding: luca.placidi@uninettunouniversity.net.

#### Abstract

Mechanical behavior of materials with granular microstructures is confounded by unique features of their grain-scale mechano-morphology, such as the tension-compression asymmetry of grain interactions and irregular grain structure. Continuum models, necessary for the macro-scale description of these materials, must link to the grain-scale behavior to describe the consequences of this mechano-morphology. Here, we consider the damage behavior of these materials based upon purely mechanical concepts utilizing energy and variational approach. Granular micromechanics is accounted through Piola's ansatz and objective kinematic descriptors obtained for grain-pair relative displacement in granular materials undergoing finite deformations. Karush-Kuhn-Tucker (KKT) type conditions that provide the evolution equations for grain-pair damage and Euler-Lagrange equations for evolution of grain-pair relative displacement are derived based upon a non-standard (hemivariational) variational approach. The model applicability is illustrated for particular form of grain-pair elastic energy and dissipation functionals through numerical examples. Results show interesting damage-induced anisotropy evolution including the emergence of a type of chiral behavior and formation of finite localization zones.

Keywords: damage mechanics, granular microstructures, variational procedure, Karush-Kuhn-Tucker conditions, strain gradient, anisotropy evolution, 2D continua

#### 1 Introduction

Material damage is a complex phenomenon that occurs over a range of spatial scales spanning molecular or crystal structures, grain boundaries and inter-granular layers, granular structures, etc. [40, 42, 71]. For example, damage can take the form of dislocation formation at atomic scales, grain boundary sliding or rupture of inter-granular layers and, at larger scales, it could consists in a coalition of complex cooperative and competing mechanisms involving a large number of microstructural units. Such mechanisms might lead to strain localization bands consisting in numerous interacting micro-fractures [6, 9, 14, 19, 26, 27, 34, 33, 36, 35, 37, 39, 49]. Clearly, the detailed description of these phenomena for a complex material system is fraught with challenges. Consequently, continuum damage models [1, 5] have been vigorously pursued (see for example the continuum-damage and phase field models [6, 10, 11, 62, 37, 36]). In recent times, many multi-scale approaches have also been proposed [15, 32]. Nevertheless, for materials as in granular solids that are suffused with varying compositions, interfaces, grain sizes and shapes, all features collectively termed as micro-mechano-morphology, continuum models informed by micromechanical considerations remain the most attractive description [41, 40, 42, 71].

In this paper, we consider the deformation behavior of solids with granular microstructures undergoing damage. In such materials, the deformation of an interacting grain-pair can be effectively described in terms of the relative movements of the grain centroids/barycenters regardless of the location of the actual deformation within the grains. The deformation energy can, therefore, be formulated in terms of this relative movement and the dissipation due to damage can be similarly considered for a grain-pair regardless of the actual sub-granular damage mechanism. The macro-scale deformation energy density of a volume of such material can then be described as an aggregation of grain-pair deformation energy and mathematically as the sum of the deformation energy of all (i.e. infinite) the grain pairs parameterized by the corresponding orientation. Such a view has shown to be a promising approach for the description of granular system whether from a discrete or continuum viewpoint (see for example a brief review in [2, 4, 18, 38, 43, 66, 68, 69]). With this view as a point of departure, we utilize a variational approach for modeling behavior of granular solids undergoing damage under finite deformations based upon grain-pair interactions. Consequently, as a first step we develop an objective kinematic descriptor for grain-pair relative displacement in the framework of strain-gradient theory linked to the placement function in deformed configuration. We adopt the usual practice in granular micromechanics (see for example [56, 40]) to decompose the objective grain-pair relative displacement into a component along the vector joining the grain centroids of a grain-pair, termed as normal component, and a component in the orthogonal direction, termed as tangent component. The strain energy and damage dissipation for a grain-pair is then defined in terms of these components of grain-pair relative displacement [59, 58] (reversible kinematical descriptors of the grain-pair interaction) and of damage variables (irreversible kinematical descriptors of the grain-pair interaction), i.e. normal and tangent damage variables. The elastic behavior of damaged material is derived from the formulated strain energy of the granular aggregate in terms of the grain-pair strain energy. As a result, relationships are obtained for standard first gradient (4th order stiffness tensor), second gradient (6th order stiffness tensor) and first-second-gradient interaction (5th order stiffness tensor) elastic moduli and their evolution with damage kinematical descriptors. Most importantly, a non-standard (hemi-)variational approach [13, 50, 53, 51, 54, 55, 52] is utilized to derive the Karush-Kuhn-Tucker (KKT) type conditions that provide the evolution equations for grain-pair damage kinematical descriptors, as well as supplementary conditions for evolution of grain-pair relative displacement in the form of Euler-Lagrange equations. The advantage of using a variational approach is that the KKT conditions and damage evolution equations are derived from first principles in a systematic manner and, therefore, yield robust criterion for loading-unloading-reloading conditions based upon purely mechanical considerations without invoking thermodynamic principles such as its 2nd law and Clausius-Duhem inequality.

We further note that for a typical granular system, the grain-pairs are oriented in various directions, which under a given macroscopic loading-sequence will experience different loading histories, and therefore, different damage evolution. Moreover, the damage evolves differently for the normal and tangent components of every grain-pair interaction. This, accompanied by the nonlinear nature of damage evolution adopted from the work on cementitious materials reported in , and the possibility of loading-unloading-reloading switch, results in strong path dependent macroscopic response of the material.

The resultant damage of a continuum material point is, therefore, not necessarily a linear function of the normal to loading surface. At any point during the loading process, the state depends upon its loading history. The rules of normality and associativity that are used in continuum damage theories, therefore, do not hold. At any point during the loading process, the state depends upon its loading history.

In the subsequent discussion, we first describe the Piola's ansatz for continuum description of granular systems and introduce objective measure of grain-pair relative displacement in a finite deformation second-gradient framework. We then introduce the grain-pair elastic energy function, and for illustration of the developed approach, give a simple expression with the caveat of tension-compression asymmetry for grain-pair. Similarly, the dissipation potential is defined with the view of asymmetric dissipation in grain-pair extension versus compression. The hemivariational approach is then described to obtain the KKT conditions and the supplementary conditions. The model applicability is illustrated through example simulations of a square plate under homogeneous (i.e., a flawless square plate) and non-homogeneous (i.e., a square plate with a flaw) deformation.

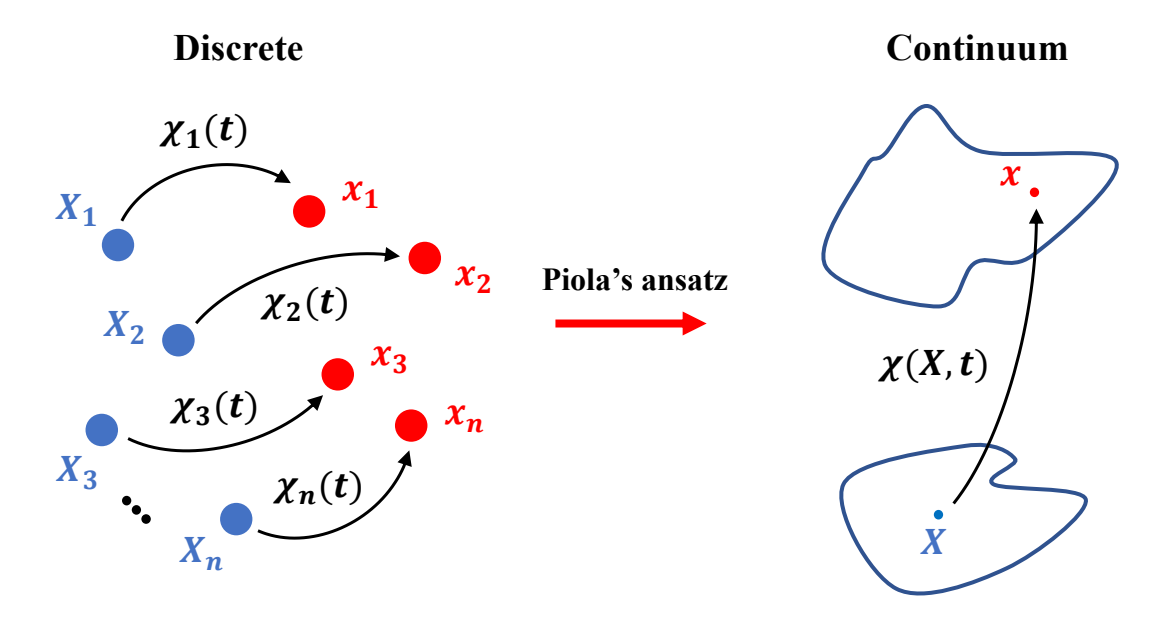


Figure 1: Piola's Ansatz. On the left-hand side a scheme with the kinematical descriptors of the discrete model. On the right-hand side a scheme with the kinematical descriptor of the continuum model.

### 2 Discrete and continuous models for granular materials

#### 2.1 Identification via Piola's ansatz

In the discrete model the reference configuration of the considered set of n grains is given by

$$\{X_1, X_2, \dots, X_n\} \in \left(E^2\right)^n,$$

where  $E^2$  is the Euclidean two dimensional space. They displace, respectively, with the following displacement functions

$$u_1(X_1) = \chi_1(X_1) - X_1, u_2(X_2) = \chi_2(X_2) - X_2, \dots, u_n(X_n) = \chi_n(X_n) - X_n,$$

where  $\chi_{i}(X_{i})$  is the placement of the *i*-th grain eventually depending on time *t*.

In the continuum model we have a continuous body  $\mathfrak{B}$  which, in the reference configuration, is constituted by infinite particles having position X, i.e.  $X \in \mathfrak{B}$ . Each particle has displacement  $u(X) = \chi(X) - X$ , where  $\chi(X)$  is the placement function of the continuous body  $\mathfrak{B}$ .

In the continuum-discrete models identification, the following Piola's Ansatz will be assumed

$$u(X_1) = u_1(X_1), \quad u(X_2) = u_2(X_2), \quad , \dots, \quad u(X_n) = u_n(X_n),$$

that means that the displacements of the n grains correspond to the displacement u(X) of the continuous body  $\mathfrak{B}$  evaluated at the points  $X_i$  with i=1,...,n where the grains are located in the reference configuration.

# 2.2 Relative inter-granular displacement and related continuum deformation measures

Let us assume that the distance between the particles at  $X_n$  and  $X_p$  is L and the unit vector  $\hat{n}$  is defined as follows,

$$X_n - X_p = \hat{n}L. \tag{1}$$

In the reference configuration, therefore, the vector attached to the position  $X_n$  and pointing the position  $X_p$  is  $\hat{n}L$  and given in (1).

In the actual configuration the positions of the two particles at  $X_n$  and  $X_p$  are, respectively,  $\chi(X_n)$  and  $\chi(X_p)$ . The vector in (1) in the present configuration yields

$$\chi\left(X_n\right) - \chi\left(X_p\right). \tag{2}$$

The difference between the vectors in (1) and (2) is called the relative displacement  $\delta^{np}$  of the two grains n and p,

$$\delta^{np} = \chi(X_n) - \chi(X_p) - (X_n - X_p) = u_n(X_n) - u_p(X_p).$$

It is a fundamental quantity in granular mechanics. However, it is not a measure for the deformation of the granular assembly (it is, e.g., not objective!). Indeed, a rigid body rotation centered at  $X_n$  produces, at the same time, a non zero relative displacement  $\delta^{np}$  but also a zero elastic strain energy. In order to define an objective relative displacement (i.e. a relative displacement that is really a measure of the contribution of the n-p pair to the deformation of the granular assembly), we proceed as follows. First we define the deformation gradient  $F = \nabla \chi$  as the gradient of the placement function. Thus, we define an objective relative displacement as

$$u^{np} = F^{T} (\chi (X_n) - \chi (X_p)) - (X_n - X_p).$$
(3)

The objectivity of  $u^{np}$  is proved by considering the facts that the matrix representation of the deformation gradient F and the column representations of the vectors  $\chi(X_n) - \chi(X_p)$  and  $X_n - X_p$  are, in a certain frame of reference, respectively,  $F_1$ ,  $\kappa_1$  and  $v_1$ . If we change the frame of reference, it is well-known that we have another matrix and other column representations, i.e.  $F_2 = QF_1$ ,  $\kappa_2 = Q\kappa_1$  and  $v_2 = v_1$ , respectively, where Q is the orthogonal matrix that makes such a change of the frame of reference. Thus, the objectivity of  $u^{np}$  is proved because in the first frame of reference its column representations is  $u_1^{np} = F_1^T \kappa_1 - v_1$  and, in the second frame of reference, the new column representation is

$$u_2^{np} = F_2^T \kappa_2 - \upsilon_2 = F_1^T Q^T Q \kappa_1 - \upsilon_1 = F_1^T \kappa_1 - \upsilon_1 = u_1^{np},$$

that is therefore independent of the frame of reference. As a matter of facts, the definition (3) of the objective relative displacement is not unique and has to be considered an assumption within the framework presented in this work. Different choices could be done, e.g. by using in (3), instead of F, its orthogonal part in a standard polar decomposition. Let us now assume that the two grains n and p are neighboring grains. Let us restrict the present model to the case that these neighboring grains also place similarly in the present configuration, and therefore the following Taylor's series expansion is possible and yields

$$\chi(X_n) = \chi(X_p) + (\nabla \chi)_{X_p} (X_n - X_p) + \frac{1}{2} \left[ (\nabla^2 \chi)_{X_p} (X_n - X_p) \right] \cdot (X_n - X_p). \tag{4}$$

It is worth to be noted that this simplification may loose its applicability for materials that possess strong variations and discontinuities of stiffnesses or have highly disordered micro-geometries, which could be deliberately designed as in pantographic metamaterials [1, 7, 17, 16, 24, 23, 21, 22, 20, 25, 28, 29, 60, 63, 64, 67] or in granular (meta)materials [44]. In these cases, Taylor's series expansion is not representative and additional kinematic descriptors may be introduced to accurately describe the response as in Cosserat or micromorphic media [30, 47].

The Green-Saint-Venant tensor G, as well as its gradient

$$G = \frac{1}{2} \left( F^T F - I \right), \quad \nabla G = F^T \nabla F, \tag{5}$$

are defined in terms of the deformation gradient F. The last three equations in (4) and (5) involve third order tensors and it is more convenient to show them in index notation

$$\chi_i^n = \chi_i^p + F_{ij}^p \hat{n}_j L + \frac{1}{2} F_{ij,h}^p \hat{n}_j \hat{n}_h L^2, \quad G_{ij}^p = \frac{1}{2} \left( F_{ai}^p F_{aj}^p - \delta_{ij} \right), \quad G_{ij,h}^p = F_{ai}^p F_{aj,h}^p, \tag{6}$$

where apexes n or p denote the relation, respectively, to the points  $X_n$  or  $X_p$ . Thus, the objective relative displacement in (3) is, in index notation,

$$u_i^{np} = F_{ai}^p \left( \chi_a^n - \chi_a^p \right) - \left( X_i^n - X_i^p \right),$$

that, from (1) and  $(6)_1$  yields

$$u_i^{np} = F_{ai}^p \left( F_{aj}^p \hat{n}_j L + \frac{1}{2} F_{aj,h}^p \hat{n}_j \hat{n}_h L^2 \right) - \hat{n}_i L,$$

that, rearranging the terms, is

$$u_i^{np} = F_{ai}^p F_{aj}^p \hat{n}_j L - \delta_{ij} \hat{n}_j L + \frac{1}{2} F_{ai}^p F_{aj,h}^p \hat{n}_j \hat{n}_h L^2,$$

where  $\delta_{ij}$  is the Kronecker symbol and, with the use of  $(6)_{2,3}$ , the previous equation yields

$$u_i^{np} = 2G_{ij}^p \hat{n}_j L + \frac{1}{2}G_{ij,h}^p \hat{n}_j \hat{n}_h L^2.$$
 (7)

The projection of the objective relative displacement on the unit vector  $\hat{n}$ , defined in (1), is the so called normal displacement  $u_{\eta}$ , that is defined,

$$u_n = u^{np} \cdot \hat{n}. \tag{8}$$

Insertion of (7) into (8) is

$$u_{\eta} = 2LG_{ij}^{p}\hat{n}_{i}\hat{n}_{j} + \frac{1}{2}L^{2}G_{ij,h}^{p}\hat{n}_{i}\hat{n}_{j}\hat{n}_{h}. \tag{9}$$

Its square is

$$u_{\eta}^{2} = \left(2LG_{ij}^{p}\hat{n}_{i}\hat{n}_{j} + \frac{1}{2}L^{2}G_{ij,h}^{p}\hat{n}_{i}\hat{n}_{j}\hat{n}_{h}\right)\left(2LG_{ab}^{p}\hat{n}_{a}\hat{n}_{b} + \frac{1}{2}L^{2}G_{ab,c}^{p}\hat{n}_{a}\hat{n}_{b}\hat{n}_{c}\right)$$

or

$$u_{\eta}^{2} = 4L^{2}\hat{n}_{i}\hat{n}_{j}\hat{n}_{a}\hat{n}_{b}G_{ij}^{p}G_{ab}^{p} + 2L^{3}\hat{n}_{i}\hat{n}_{j}\hat{n}_{a}\hat{n}_{b}\hat{n}_{c}G_{ij}^{p}G_{ab,c}^{p} + \frac{1}{4}L^{4}\hat{n}_{i}\hat{n}_{j}\hat{n}_{h}\hat{n}_{a}\hat{n}_{b}\hat{n}_{c}G_{ij,h}^{p}G_{ab,c}^{p}.$$
(10)

The objective relative displacement vector  $u^{np}$  projected orthogonally to  $\hat{n}$ , i.e. the unit vector defined in (1), is the so called tangential displacement  $u_{\tau}$ , that is a vector and therefore defined,

$$u_{\tau} = u^{np} - (u^{np} \cdot \hat{n}) \,\hat{n}. \tag{11}$$

The tangential displacement  $u_{\tau}$  is a vector. The only objective quantity derived from  $u_{\tau}$  and  $\hat{n}$  is the square of  $u_{\tau}$ , i.e.

$$u_{\tau}^{2} = (u^{np} - (u^{np} \cdot \hat{n}) \,\hat{n}) \cdot (u^{np} - (u^{np} \cdot \hat{n}) \,\hat{n}) = u^{np} \cdot u^{np} - (u^{np} \cdot \hat{n})^{2}$$
(12)

or, in index notation,

$$u_{\tau}^{2} = \left(2G_{ij}^{p}\hat{n}_{j}L + \frac{1}{2}G_{ij,h}^{p}\hat{n}_{j}\hat{n}_{h}L^{2}\right)\left(2G_{ik}^{p}\hat{n}_{k}L + \frac{1}{2}G_{im,n}^{p}\hat{n}_{m}\hat{n}_{n}L^{2}\right) - u_{\eta}^{2},\tag{13}$$

that means

$$u_{\tau}^{2} + u_{\eta}^{2} = 4L^{2}G_{ij}^{p}G_{ik}^{p}\hat{n}_{j}\hat{n}_{k} + 2L^{3}G_{ij}^{p}G_{im,n}^{p}\hat{n}_{j}\hat{n}_{m}\hat{n}_{n} + \frac{1}{4}L^{4}G_{ij,h}^{p}G_{im,n}^{p}\hat{n}_{j}\hat{n}_{h}\hat{n}_{m}\hat{n}_{n}$$

or, taking (10) into account,

$$u_{\tau}^{2} = 4L^{2}G_{ij}^{p}G_{ab}^{p}\left(\delta_{ia}\hat{n}_{j}\hat{n}_{b} - \hat{n}_{i}\hat{n}_{j}\hat{n}_{a}\hat{n}_{b}\right) + 2L^{3}G_{ij}^{p}G_{ab,c}^{p}\left(\delta_{ia}\hat{n}_{j}\hat{n}_{b}\hat{n}_{c} - \hat{n}_{i}\hat{n}_{j}\hat{n}_{a}\hat{n}_{b}\hat{n}_{c}\right) + \frac{1}{4}L^{4}G_{ij,h}^{p}G_{am,n}^{p}\left(\delta_{ia}\hat{n}_{j}\hat{n}_{h}\hat{n}_{m}\hat{n}_{n} - \hat{n}_{i}\hat{n}_{j}\hat{n}_{h}\hat{n}_{a}\hat{n}_{b}\hat{n}_{c}\right).$$

$$(14)$$

#### 2.3 Damage and stiffnesses

The damaged normal stiffness is driven by the sign of the objective normal displacement. In tension (i.e. for positive normal displacement) it is

$$k_{n,D}^t$$

In compression (i.e. for negative normal displacement) it is higher for cementitious granular materials

$$k_{\eta,D}^c \gg k_{\eta,D}^t$$

In order to give a synthetic expression for the damaged normal stiffness  $k_{\eta,D}$  we use the Heaviside function H,

$$k_{\eta,D} = k_{\eta,D}^t H(u_{\eta}) + k_{\eta,D}^c H(-u_{\eta})$$
(15)

The damaged tangent stiffness  $k_{\tau,D}$ 

$$k_{\tau,D}$$
. (16)

is, on the other hand, the same for both directions.

Damage is modeled with two variables, i.e. the normal damage

$$D_{\eta}, \tag{17}$$

and the tangent damage

$$D_{\tau}$$
. (18)

In the earlier model presented by Misra and coworkers [40, 39, 41, 42], such quantities take the role, respectively, of  $D_n^{max}$  and  $D_w^{max}$ . The damage variables in (17) and (18) have the role to reduce (respectively), the normal (15) and the tangent (16) stiffnesses as follows

$$k_{\eta,D}^{t} = k_{\eta}^{t} (1 - D_{\eta}), \qquad k_{\eta,D}^{c} = k_{\eta}^{c} (1 - D_{\eta}), \qquad k_{\tau,D} = k_{\tau} (1 - D_{\tau})$$
 (19)

that means both that the damaged tangent stiffness  $k_{\tau,D}$  is defined by the non-damaged tangent stiffness  $k_{\tau}$  and that the damaged normal stiffness  $k_{\eta,D}$  is defined by the non-damaged normal stiffness  $k_{\eta}$ ,

$$k_{\eta,D} = k_{\eta} \left( 1 - D_{\eta} \right).$$

Besides, the non-damaged normal stiffness  $k_{\eta}$  is defined in terms of the non-damaged tension normal stiffness  $k_{\eta}^{t}$  and the non-damaged compression normal stiffness  $k_{\eta}^{c}$ ,

$$k_{\eta} = k_{\eta}^{t} H\left(u_{\eta}\right) + k_{\eta}^{c} H\left(-u_{\eta}\right), \tag{20}$$

that finally yields,

$$k_{\eta,D} = k_{\eta} (1 - D_{\eta}) = k_{\eta}^{t} (1 - D_{\eta}) H (u_{\eta}) + k_{\eta}^{c} (1 - D_{\eta}) H (-u_{\eta}).$$
(21)

# 3 Elastic energy function

The elastic energy function for a given couple of grains, say the couple n-p considered in Subsection 2.2, is assumed to be, in the discrete and (because of the Piola's Ansatz) in the continuum models, a quadratic form of normal and tangent parts components of the objective relative displacement,

$$U = \frac{1}{2}k_{\eta} (1 - D_{\eta}) u_{\eta}^{2} + \frac{1}{2}k_{\tau} (1 - D_{\tau}) u_{\tau}^{2},$$
(22)

where  $u_{\eta}^2$  is the square of the scalar  $u_{\eta}$  and  $u_{\tau}^2$  is the squared module of the vector  $u_{\tau}$ . In this simple form of the elastic energy function, the coupling term between  $u_{\eta}$  and  $u_{\tau}$  is ignored, as also the linear terms with respect to  $u_{\eta}$  and  $u_{\tau}$  and finally the dependency of the energy upon gradients of the objective relative displacement components. The reason for the first omission is that  $u_{\tau}$  is a vector and the only objective quantity that we can build to generate from it an elastic strain energy contribution is given by its square  $u_{\tau}^2$ . Besides, a linear term with respect to the scalar  $u_{\eta}$  is also neglected. The reason is that it is possibile to prove that it changes the stress-free reference configuration. Thus, we will consider it in the future in order to take plasticity into account. Finally, for materials with complex microstructures, the Piola's Ansatz could be constructed by considering in a different way the critical representative grains. In these cases, the grain-pair deformation energy function in (22) may not only depend upon the objective relative displacement, but also on its gradients or additional kinematic parameters (or descriptors). Indeed, this is clear if the critical grain-pair interactions were those akin to a pantograph, e.g. analyzed in [3, 61], or when many complex mechanisms result in the need to introduce additional kinematical descriptors to capture the deformation energy of grain-pair [31, 47, 57]. In these cases, the boundary layers and localization thicknesses that emerge during nonhomogeneous deformation are effected by the energy stored and dissipated in the gradient terms, and typically, result in layers of thicknesses that are multiples of grain-sizes (we intend to illustrate these points in forthcoming publications) or of the inter-granular distance L.

The total energy  $U^{tot}$  for a given particle at  $X_p$  is the sum of the energy in (22) over all the N possible interactions, i.e. between the grain p and all the N neighboring grains n,

$$U^{tot} = \sum_{i=1}^{N} \left[ \frac{1}{2} k_{\eta;i} \left( 1 - D_{\eta;i} \right) u_{\eta;i}^{2} + \frac{1}{2} k_{\tau;i} \left( 1 - D_{\tau;i} \right) u_{\tau;i}^{2} \right], \tag{23}$$

where the subscript i refers to a single couple of grains of the type n-p. In (23) it is therefore intended that  $k_{\eta;i}$  is the non-damaged normal stiffness for the i-th couple of grains,  $k_{\tau;i}$  is the non-damaged tangent stiffness for the i-th couple of grains,  $D_{\eta;i}$  is the normal damage for the i-th couple of grains,  $D_{\tau;i}$  is the tangent damage for the i-th couple of grains,  $u_{\eta;i}$  is the scalar normal relative displacement for the i-th couple of grains and  $u_{\tau;\eta i}^2$  is the squared tangent displacement for the i-th couple of grains.

Continuization of Eq. (23) is done by the use of the following homogenization rule explicited for a general quantity a, represented with  $a_i$  for the *i*-th couple of grains of the type n-p in the discrete model and with  $a(\theta)$  for the orientation  $\theta$  (corresponding to the unit vector from the particle p to the particle n in the discrete model) in the continuum model,

$$\sum_{i=1}^{N} [a_i] \longrightarrow \int_{\mathcal{S}^1} a(\theta). \tag{24}$$

where  $S^1 = [0, 2\pi]$  is the unit circle, domain of the function  $a(\theta)$ , i.e. the set of all the orientations. The use of the homogenization rule in (24) for total energy  $U^{tot}$  in (23) yields

$$U = \int_{\mathcal{S}^1} \frac{1}{2} k_{\eta} (1 - D_{\eta}) u_{\eta}^2 + \frac{1}{2} k_{\tau} (1 - D_{\tau}) u_{\tau}^2, \tag{25}$$

where  $k_{\eta} = \widetilde{k}_{\eta}(\theta)$ ,  $k_{\tau} = \widetilde{k}_{\tau}(\theta)$ ,  $D_{\eta} = \widetilde{D}_{\eta}(\theta)$  and  $D_{\tau} = \widetilde{D}_{\tau}(\theta)$  substitute, respectively,  $k_{\eta,i} k_{\tau,i} D_{\eta,i}$  and  $D_{\tau,i}$ , and are all functions of that orientation  $\theta \in [0, 2\pi]$  connected with the orientation  $\hat{n}$  of the *i*-th couple of grains, that yields the following identification rules,

$$k_{\eta,i} \to \widetilde{k}_{\eta}(\theta), \quad k_{\tau,i} \to \widetilde{k}_{\tau}(\theta), \quad D_{\eta,i} \to \widetilde{D}_{\eta}(\theta), \quad D_{\tau,i} \to \widetilde{D}_{\tau}(\theta).$$

From (10) and (14), the elastic strain energy of the granular aggregate (25) is

$$U = \int_{S^{1}} \frac{1}{2} k_{\eta} (1 - D_{\eta}) \left( 4L^{2} \hat{n}_{i} \hat{n}_{j} \hat{n}_{a} \hat{n}_{b} G_{ij} G_{ab} + 2L^{3} \hat{n}_{i} \hat{n}_{j} \hat{n}_{a} \hat{n}_{b} \hat{n}_{c} G_{ij} G_{ab,c} \right)$$

$$+ \int_{S^{1}} \frac{1}{2} k_{\eta} (1 - D_{\eta}) \left( \frac{1}{4} L^{4} \hat{n}_{i} \hat{n}_{j} \hat{n}_{h} \hat{n}_{a} \hat{n}_{b} \hat{n}_{c} G_{ij,h} G_{ab,c} \right)$$

$$+ \int_{S^{1}} \frac{1}{2} k_{\tau} (1 - D_{\tau}) \left( 4L^{2} G_{ij} G_{ab} \left( \delta_{ia} \hat{n}_{j} \hat{n}_{b} - \hat{n}_{i} \hat{n}_{j} \hat{n}_{a} \hat{n}_{b} \right) + 2L^{3} G_{ij} G_{ab,c} \left( \delta_{ia} \hat{n}_{j} \hat{n}_{b} \hat{n}_{c} - \hat{n}_{i} \hat{n}_{j} \hat{n}_{a} \hat{n}_{b} \hat{n}_{c} \right) \right)$$

$$+ \int_{S^{1}} \frac{1}{2} k_{\tau} (1 - D_{\tau}) \left( \frac{1}{4} L^{4} G_{ij,h} G_{ab,c} \left( \delta_{ia} \hat{n}_{j} \hat{n}_{h} \hat{n}_{b} \hat{n}_{c} - \hat{n}_{i} \hat{n}_{j} \hat{n}_{h} \hat{n}_{a} \hat{n}_{b} \hat{n}_{c} \right) \right). \tag{26}$$

or, in a compact form is

$$U = \frac{1}{2} \mathbb{C}_{ijab} G_{ij} G_{ab} + \mathbb{M}_{ijabc} G_{ij} G_{ab,c} + \frac{1}{2} \mathbb{D}_{ijhabc} G_{ij,h} G_{ab,c}, \tag{27}$$

where the apexes p have all been omitted and the elastic stiffnesses  $\mathbb{C}$ ,  $\mathbb{M}$  and  $\mathbb{D}$  are identified in (27) as follows, with the symmetrization induced by the symmetry of the strain tensor G,

$$\mathbb{C}_{ijab} = 4L^{2} \int_{\mathcal{S}^{1}} k_{\eta} (1 - D_{\eta}) \hat{n}_{i} \hat{n}_{j} \hat{n}_{a} \hat{n}_{b} 
+ 4L^{2} \int_{\mathcal{S}^{1}} k_{\tau} (1 - D_{\tau}) \left( \frac{1}{4} (\delta_{ia} \hat{n}_{j} \hat{n}_{b} + \delta_{ib} \hat{n}_{j} \hat{n}_{a} + \delta_{ja} \hat{n}_{i} \hat{n}_{b} + \delta_{jb} \hat{n}_{i} \hat{n}_{a}) - \hat{n}_{i} \hat{n}_{j} \hat{n}_{a} \hat{n}_{b} \right) 
\mathbb{M}_{ijabc} = L^{3} \int_{\mathcal{S}^{1}} k_{\eta} (1 - D_{\eta}) \hat{n}_{i} \hat{n}_{j} \hat{n}_{a} \hat{n}_{b} \hat{n}_{c} 
+ L^{3} \int_{\mathcal{S}^{1}} k_{\tau} (1 - D_{\tau}) \left( \frac{1}{4} (\delta_{ia} \hat{n}_{j} \hat{n}_{b} + \delta_{ib} \hat{n}_{j} \hat{n}_{a} + \delta_{ja} \hat{n}_{i} \hat{n}_{b} + \delta_{jb} \hat{n}_{i} \hat{n}_{a}) \hat{n}_{c} - \hat{n}_{i} \hat{n}_{j} \hat{n}_{a} \hat{n}_{b} \hat{n}_{c} \right) 
\mathbb{D}_{ijhabc} = \frac{1}{4} L^{4} \int_{\mathcal{S}^{1}} k_{\eta} (1 - D_{\eta}) \hat{n}_{i} \hat{n}_{j} \hat{n}_{h} \hat{n}_{a} \hat{n}_{b} \hat{n}_{c} 
+ \frac{1}{4} L^{4} \int_{\mathcal{S}^{1}} k_{\tau} (1 - D_{\tau}) \left( \frac{1}{4} (\delta_{ia} \hat{n}_{j} \hat{n}_{b} + \delta_{ib} \hat{n}_{j} \hat{n}_{a} + \delta_{ja} \hat{n}_{i} \hat{n}_{b} + \delta_{jb} \hat{n}_{i} \hat{n}_{a}) \hat{n}_{h} \hat{n}_{c} - \hat{n}_{i} \hat{n}_{j} \hat{n}_{h} \hat{n}_{a} \hat{n}_{b} \hat{n}_{c} \right)$$
(30)

Assuming small displacement (and small displacement gradient) approximation means quadratic approximation of the strain energy with respect to the displacement gradient H and to its symmetric part E defined as follows,

$$H = \nabla u, \quad E = \frac{1}{2} (H + H^T),$$

that yields

$$U = \frac{1}{2} \mathbb{C}_{ijab} E_{ij} E_{ab} + \mathbb{M}_{ijabc} E_{ij} E_{ab,c} + \frac{1}{2} \mathbb{D}_{ijhabc} E_{ij,h} E_{ab,c}, \tag{31}$$

The elastic stiffnesses in Eqs. (28), (29) and (30), indicate that the regularization length-scale in this model is of the order of the inter-granular distance L, which is a consequence of the assumed grain-pair energy (see Eq. (22) and the discussion thereafter), an assumption often made in discrete-continuum identifications (see for example [12, 65]). As suggested in our above discussion, enriched grain-pair energy that includes effect of gradients are needed such that the regularization lengths can properly represent all the grain-scale (micro-scale) deformation mechanisms. We finally remark that the strain gradient approximation induced by the Taylor's series expansion in (4) and the presence of damage, induce a chiral effect on the granular assembly deduced by the non trivial form in (29) of the stiffness  $\mathbb{M}$ . The reason is that, in the integral in (29), the unit vector  $\hat{n}$  appears an odd number of times and the domain is even. Thus, on the one hand and for damage-free materials where non-damaged stiffness  $k_{\eta}$  and  $k_{\tau}$  are independent on the versus of the unit vector  $\hat{n}$ , we have  $\mathbb{M} = 0$ . On the other hand, an evolution of damage variables  $D_{\eta}$  and  $D_{\tau}$  that is non-symmetric with respect to the sign of  $\hat{n}$  induces a chiral effect evidenced by the condition  $\mathbb{M} \neq 0$ .

## 4 Identification of the damage-free isotropic case

#### 4.1 Macroscopic stiffnesses matrices

Isotropic standard representation of the 4th order stiffness tensor for both 2D and 3D cases is

$$\mathbb{C}_{ijab} = \mu \delta_{ia} \delta_{jb} + \mu \delta_{ib} \delta_{ja} + \lambda \delta_{ij} \delta_{ab} \tag{32}$$

$$\mathbb{C}_{1111} = \lambda + 2\mu \tag{33}$$

$$\mathbb{C}_{1122} = \lambda \tag{34}$$

Thus, an identification of 2D or 3D Lamé coefficients in terms of the stiffness matrix components is as follows

$$\lambda = \mathbb{C}_{1122}, \qquad \mu = \frac{1}{2} \left( \mathbb{C}_{1111} - \mathbb{C}_{1122} \right).$$
 (35)

Besides, the 4 independent strain gradient isotropic elastic coefficients in the 2D case are here reported in the nomenclature of [8], i.e.,

$$a_{11} = \mathbb{D}_{111111}, \quad a_{22} = \mathbb{D}_{221221}, \quad a_{12} = \mathbb{D}_{111221}, \quad a_{23} = \sqrt{2}\mathbb{D}_{221122}.$$
 (36)

#### 4.2 Microscopic stiffnesses matrices

In the 2D case, a standard representation of the unit vector is

$$n_1 = \cos \theta, \ n_2 = \sin \theta, \tag{37}$$

where  $\theta$  is the anti-clockwise angle from the first unit vector  $\hat{e}_1$  of the frame of reference to  $\hat{n}$ . Besides, trivial analytical results are as follows

$$\int_0^{2\pi} \sin^2 \theta d\theta = \int_0^{2\pi} \cos^2 \theta d\theta = \pi,$$

$$\int_0^{2\pi} \sin^2 \theta \cos^2 d\theta = \frac{1}{4}\pi$$

$$\int_0^{2\pi} \sin^4 \theta d\theta = \int_0^{2\pi} \cos^4 \theta d\theta = \frac{3}{4}\pi.$$

$$\int_0^{2\pi} \sin^6 \theta d\theta = \int_0^{2\pi} \cos^6 \theta d\theta = \frac{5}{8}\pi$$

The components  $\mathbb{C}_{1111}$  and  $\mathbb{C}_{1122}$  are, from (28) and (37), and no damage condition  $D_{\eta} = D_{\tau} = 0$ ,

$$\mathbb{C}_{1111} = 4L^2 \int_0^{2\pi} \left[ \tilde{k}_{\eta} (\theta) \cos^4 \theta + \tilde{k}_{\tau} (\theta) \left( \cos^2 \theta - \cos^4 \theta \right) \right] = 
= \frac{4L^2}{2\pi} \left[ \left( \bar{k}_{\eta} - \bar{k}_{\tau} \right) \frac{3}{4} \pi + \bar{k}_{\tau} \pi \right] = \frac{L^2}{2} \left( 3\bar{k}_{\eta} + \bar{k}_{\tau} \right).$$
(38)

$$\mathbb{C}_{1122} = 4L^2 \int_0^{2\pi} \left[ \widetilde{k}_{\eta} \left( \theta \right) \sin^2 \theta \cos^2 \theta + \widetilde{k}_{\tau} \left( \theta \right) \left( -\sin^2 \theta \cos^2 \theta \right) \right] = \tag{39}$$

$$=\frac{4L^2}{2\pi}\left[\left(\bar{k}_{\eta}-\bar{k}_{\tau}\right)\frac{1}{4}\pi\right]=\frac{L^2}{2}\left(\bar{k}_{\eta}-\bar{k}_{\tau}\right),\,$$

$$\mathbb{D}_{111111} = \frac{1}{4} L^4 \int_0^{2\pi} \left[ \widetilde{k}_{\eta} \left( \theta \right) \cos^6 \theta + \widetilde{k}_{\tau} \left( \theta \right) \left( \cos^4 \theta - \cos^6 \theta \right) \right] \tag{40}$$

$$=\frac{L^4}{8\pi}\left[\left(\bar{k}_{\eta}-\bar{k}_{\tau}\right)\frac{5}{8}\pi+\bar{k}_{\tau}\frac{3}{4}\pi\right]=\frac{L^4}{64}\left[5\bar{k}_{\eta}+\bar{k}_{\tau}\right]$$

$$\mathbb{D}_{221221} = \frac{1}{4} L^4 \int_0^{2\pi} \left[ \widetilde{k}_{\eta} \left( \theta \right) \sin^4 \theta \cos^2 \theta + \widetilde{k}_{\tau} \left( \theta \right) \left( \sin^2 \theta \cos^2 \theta - \sin^4 \theta \cos^2 \theta \right) \right] \tag{41}$$

$$= \frac{1}{8\pi} L^4 \left[ \left( \bar{k}_{\eta} - \bar{k}_{\tau} \right) \frac{\pi}{8} + \bar{k}_{\tau} \frac{1}{4} \pi \right] = \frac{L^4}{64} \left[ \bar{k}_{\eta} + \bar{k}_{\tau} \right]$$

$$\mathbb{D}_{111221} = \frac{1}{4} L^4 \int_0^{2\pi} \left[ \widetilde{k}_{\eta} \left( \theta \right) \sin^2 \theta \cos^4 \theta + \widetilde{k}_{\tau} \left( \theta \right) \left( -\sin^2 \theta \cos^4 \theta \right) \right] \tag{42}$$

$$=\frac{1}{8\pi}L^4\left[\left(\bar{k}_{\eta}-\bar{k}_{\tau}\right)\frac{\pi}{8}\right]=\frac{L^4}{64}\left[\bar{k}_{\eta}-\bar{k}_{\tau}\right]$$

$$\mathbb{D}_{221122} = \frac{1}{4} L^4 \int_0^{2\pi} \left[ \widetilde{k}_{\eta} \left( \theta \right) \sin^4 \theta \cos^2 \theta + \widetilde{k}_{\tau} \left( \theta \right) \left( \frac{1}{2} \sin^2 \theta \cos^2 \theta - \sin^4 \theta \cos^2 \theta \right) \right]$$
(43)

$$= \frac{1}{8\pi} L^4 \left[ \left( \bar{k}_{\eta} - \bar{k}_{\tau} \right) \frac{\pi}{8} + \bar{k}_{\tau} \frac{\pi}{8} \right] = \frac{L^4}{64} \bar{k}_{\eta}$$

where the isotropic condition has been imposed by assuming (i) no dependence of  $k_{\eta}$  and  $k_{\tau}$  with respect to  $\hat{n}$  (or  $\theta$ ), (ii)

$$\widetilde{k}_{\eta}\left(\theta\right) = \frac{\bar{k}_{\eta}}{2\pi}, \qquad \widetilde{k}_{\tau}\left(\theta\right) = \frac{\bar{k}_{\tau}}{2\pi},$$

where  $\bar{k}_{\eta}$  and  $\bar{k}_{\tau}$  are the integrated stiffness over the set of possible orientations, that are defined in the general anisotropic case as follows,

$$\bar{k}_{\eta} = \int_{0}^{2\pi} \widetilde{k}_{\eta}(\theta) d\theta, \qquad \bar{k}_{\tau} = \int_{0}^{2\pi} \widetilde{k}_{\tau}(\theta) d\theta.$$

#### 4.3 Isotropic micro-macro Identification

By comparing (35), (38) and (39), we obtain the following identification of the 2D Lamé coefficients in terms of normal and tangent stiffness

$$\mu = \frac{L^2}{2} \left( \bar{k}_{\eta} + \bar{k}_{\tau} \right), \qquad \lambda = \frac{L^2}{2} \left( \bar{k}_{\eta} - \bar{k}_{\tau} \right).$$

In the 2D model, Young module Y and Poisson module  $\nu$  are

$$Y = 4\mu \frac{\lambda + \mu}{\lambda + 2\mu}, \quad \nu = \frac{\lambda}{2(\lambda + \mu)}.$$

Thus an identification of Young and Poisson modules are as follows,

$$Y = 4L^{2}\bar{k}_{\eta}\frac{\bar{k}_{\eta} + \bar{k}_{\tau}}{3\bar{k}_{\eta} + \bar{k}_{\tau}}, \quad \nu = \frac{\bar{k}_{\eta} - \bar{k}_{\tau}}{4\bar{k}_{\eta}}$$

By comparing (36), (40), (41), (42) and (43), we obtain the following identification of the 4 2D strain gradient coefficients in terms of normal and tangent stiffness,

$$a_{11} = \frac{L^4}{64} \left[ 5\bar{k}_\eta + \bar{k}_\tau \right], \quad a_{22} = \frac{L^4}{64} \left[ \bar{k}_\eta + \bar{k}_\tau \right], \quad a_{12} = \frac{L^4}{64} \left[ \bar{k}_\eta - \bar{k}_\tau \right], \quad a_{23} = \frac{L^4}{64} \sqrt{2} \bar{k}_\eta.$$

#### 5 Evolution of damage

#### 5.1 Definition of the fundamental kinematical quantities

We evaluate the evolution of damage variables via an hemi-variational derivation of the grain interaction, that is considered for a given orientation. To do this, we start by the definition of the following 4 (3 scalar and one vector) fundamental kinematical quantities

$$u_{\eta}, u_{\tau}, D_{\eta}, D_{\tau}, \tag{44}$$

where  $u_{\eta}$ ,  $u_{\tau}$ ,  $D_{\eta}$  and  $D_{\tau}$  have been already defined in (8), (11), (17) and (18).

#### 5.2 Definition of the dissipation, external and total energy functionals

The damage dissipation energy functional W is assumed to be additively decomposed into normal, i.e.  $W^{\eta}$ , and tangent, i.e.  $W^{\tau}$ , coupled parts,

$$W = W^{\eta} + W^{\tau}. \tag{45}$$

The assumption of the normal contribution  $W^{\eta}$  is as follows

$$W^{\eta} = \frac{1}{2} k_{\eta}^{c} \left( B_{\eta}^{c} \right)^{2} H \left( -u_{\eta} \right) \left[ -D_{\eta} + \frac{2}{\pi} \tan \left( \frac{\pi}{2} D_{\eta} \right) \right] +$$

$$\frac{1}{2} k_{\eta}^{t} \left( B_{\eta}^{t} \right)^{2} H \left( u_{\eta} \right) \left[ 2 + \left( D_{\eta} - 1 \right) \left( 2 - 2 \log \left( 1 - D_{\eta} \right) + \left( \log \left( 1 - D_{\eta} \right) \right)^{2} \right) \right],$$

$$(46)$$

where  $B_{\eta}^{c}$  and  $B_{\eta}^{t}$  are the characteristic lengths for the normal damage dissipation, respectively, in compression and in tension. Besides, the assumption of the tangent contribution  $W^{\tau}$  is

$$W^{\tau} = \frac{1}{2} k_{\tau} \left[ \widetilde{B}_{\tau} \left( u_{\eta} \right) \right]^{2} \left[ 2 + \left( D_{\tau} - 1 \right) \left( 2 - 2 \log \left( 1 - D_{\tau} \right) + \left( \log \left( 1 - D_{\tau} \right) \right)^{2} \right) \right], \tag{47}$$

where  $B_{\tau} = B_{\tau}(u_{\eta})$  is the characteristic length for the tangent damage dissipation. According to [40, 42],  $B_{\tau}$  is assumed to depend on the normal displacement  $u_{\eta}$  and, for the sake of simplicity, the effect of the mean stress has been neglected and this functional dependence has been made explicit as follows,

$$B_{\tau} = \widetilde{B}_{\tau} (u_{\eta}) = \begin{cases} B_{\tau 0}, & u_{\eta} \ge 0, \\ B_{\tau 0} - \alpha_{2} u_{\eta}, & \frac{1 - \alpha_{1}}{\alpha_{2}} B_{\tau 0} \le u_{\eta} < 0, \\ \alpha_{1} B_{\tau 0}, & u_{\eta} < B_{\tau 0} \frac{1 - \alpha_{1}}{\alpha_{2}}, \end{cases}$$
(48)

where  $B_{\tau 0}$  ( $B_{w0}$  in [40, 42]),  $\alpha_1$  and  $\alpha_2$  are further constitutive parameters that complete the functional dependence  $\tilde{B}_{\tau}(u_{\eta})$ . The forms of the dissipation energies in (46) and in (47) have been assumed in order to be coherent with the assumptions in [40, 42], and are considered to be reasonable for concrete.

The external world can exert forces expending power both on the scalar normal and on the vector tangent objective relative displacements, so that the external energy functional is

$$U^{ext} = F_{\eta}^{ext} u_{\eta} + F_{\tau}^{ext} \cdot u_{\tau}, \tag{49}$$

where  $F_{\eta}^{ext}$  and  $F_{\tau}^{ext}$  are, respectively, the external scalar normal and vector tangent external forces. The action functional  $\mathcal{E}$  is

$$\mathcal{E} = \int_{T_0}^{T_N} U + W - U^{ext} \tag{50}$$

is a functional of the fundamental kinematical quantities (44)

$$\mathcal{E} = \tilde{\mathcal{E}} \left( u_n, u_\tau, D_n, D_\tau \right) \tag{51}$$

and the initial  $T_0$  and final  $T_N$  instants of time will be defined in the next subsection.

#### 5.3 The formulation of the variational inequality principle

Let

$$T_t \in \{T_t\}_{t=0,\dots,N}$$

with

$$T_t \in \mathbb{R}, \qquad N \in \mathbb{N}$$

and

$$\{T_t\}$$

be a monotonously increasing sequence. An initial datum on the fundamental kinematical quantities must be assumed at t = 0 for time  $T_0$ .

A motion is defined as a family of displacements

$$\zeta = (u_{\eta}, u_{\tau}) \tag{52}$$

for times

$$t = 1, \ldots, N$$
.

The set  $AM_t$  is that of kinematically admissible displacements (52) and the set  $AV_t$  is that of their admissible variations,

$$v = (\delta u_{\eta}, \delta u_{\tau}) \in AV_t.$$

The admissible variation of the irreversible kinematical quantities

$$(D_{\eta}, D_{\tau})$$

are all the positive real numbers. Thus,

$$\beta = (\delta D_{\eta}, \delta D_{\tau}) \in \mathbb{R}^{+2}.$$

The variation  $\delta \mathcal{E}$ 

$$\delta \mathcal{E} = \tilde{\mathcal{E}} \left( u_{\eta} + \delta u_{\eta}, u_{\tau} + \delta u_{\tau}, D_{\eta} + \delta D_{\eta}, D_{\tau} + \delta D_{\tau} \right) - \tilde{\mathcal{E}} \left( u_{\eta}, u_{\tau}, D_{\eta}, D_{\tau} \right)$$

of the energy functional (51) evaluated at the fundamental kinematical quantities (44) along the direction

$$(\delta u_{\eta}, \delta u_{\tau}, \delta D_{\eta}, \delta D_{\tau})$$

is denoted by

$$\delta \mathcal{E} = \left\langle \tilde{\mathcal{E}}' \left( u_{\eta}, u_{\tau}, D_{\eta}, D_{\tau} \right), \left( \delta u_{\eta}, \delta u_{\tau}, \delta D_{\eta}, \delta D_{\tau} \right) \right\rangle.$$

The increment

$$(\Delta u_n, \Delta u_\tau, \Delta D_n, \Delta D_\tau)$$

at  $T_t$  is given by the fundamental kinematical quantities (44) at  $T_t$  minus the same quantities (44) at  $T_{t-1}$ , i.e.,

$$(\Delta u_{\eta}, \Delta u_{\tau}, \Delta D_{\eta}, \Delta D_{\tau})_t = (u_{\eta}, u_{\tau}, D_{\eta}, D_{\tau})_t - (u_{\eta}, u_{\tau}, D_{\eta}, D_{\tau})_{t-1}.$$

The hemivariational principle is formulated as follows. The following variational inequality holds

$$\left\langle \tilde{\mathcal{E}}'\left(u_{\eta}, u_{\tau}, D_{\eta}, D_{\tau}\right), \left(\Delta u_{\eta}, \Delta u_{\tau}, \Delta D_{\eta}, \Delta D_{\tau}\right) \right\rangle \leq$$

$$\leq \left\langle \tilde{\mathcal{E}}'\left(u_{\eta}, u_{\tau}, D_{\eta}, D_{\tau}\right), \left(\delta u_{\eta}, \delta u_{\tau}, \delta D_{\eta}, \delta D_{\tau}\right) \right\rangle$$

$$= \left\langle \tilde{\mathcal{E}}'\left(u_{\eta}, u_{\tau}, D_{\eta}, D_{\tau}\right), \left(v, \beta\right) \right\rangle$$
(53)

$$\forall \upsilon = (\delta u_{\eta}, \delta u_{\tau}) \in AV_t, \quad \forall \beta = (\delta D_{\eta}, \delta D_{\tau}) \in \mathbb{R}^{+2},$$

where the prefix "hemi" means half and recall the fact that we are using an inequality.

#### 5.4 Derivation of the Euler-Lagrange equations

Insertion of (22), (49) into (50) yields

$$\begin{split} &\mathcal{E}\left(u_{\eta}, u_{\tau}, D_{\eta}, D_{\tau}\right) = \\ &= \int_{t_{i}}^{t_{f}} \frac{1}{2} k_{\eta} \left(1 - D_{\eta}\right) u_{\eta}^{2} + \frac{1}{2} k_{\tau} \left(1 - D_{\tau}\right) u_{\tau}^{2} \\ &\frac{1}{2} k_{\eta}^{c} \left(B_{\eta}^{c}\right)^{2} H\left(-u_{\eta}\right) \left[-D_{\eta} + \frac{2}{\pi} \tan\left(\frac{\pi}{2}D_{\eta}\right)\right] \\ &+ \frac{1}{2} k_{\eta}^{t} \left(B_{\eta}^{t}\right)^{2} H\left(u_{\eta}\right) \left[2 + \left(D_{\eta} - 1\right) \left(2 - 2\log\left(1 - D_{\eta}\right) + \left(\log\left(1 - D_{\eta}\right)\right)^{2}\right)\right] \\ &+ \frac{1}{2} k_{\tau} B_{\tau}^{2} \left[2 + \left(D_{\tau} - 1\right) \left(2 - 2\log\left(1 - D_{\tau}\right) + \left(\log\left(1 - D_{\tau}\right)\right)^{2}\right)\right] \\ &- F_{\eta}^{ext} u_{\eta} - F_{\tau}^{ext} u_{\tau} \end{split}$$

so that the two members in the inequality principle (53) are

$$\begin{split} &\langle \mathcal{E}'\left(u_{\eta},u_{\tau},D_{\eta},D_{\tau}\right),\left(\Delta u_{\eta},\Delta u_{\tau},\Delta D_{\eta},\Delta D_{\tau}\right)\rangle = \\ &= \int\limits_{t_{i}}^{t_{f}} \left\{k_{\eta}\left(1-D_{\eta}\right)u_{\eta}+k_{\tau}B_{\tau}\frac{\partial \widetilde{B}_{\tau}}{\partial u_{\eta}}\int\limits_{0}^{D_{\tau}}\left[Log\left(1-x\right)\right]^{2}dx-F_{\eta}^{ext}\right\}\Delta u_{\eta} \\ &+\left\{k_{\tau}\left(1-D_{\tau}\right)u_{\tau}-F_{\tau}^{ext}\right\}\cdot\Delta u_{\tau} \\ &-\frac{1}{2}k_{\eta}u_{\eta}^{2}\Delta D_{\eta} \\ &+\frac{1}{2}k_{\eta}^{c}\left(B_{\eta}^{c}\right)^{2}H\left(-u_{\eta}\right)\left[-1+\frac{2}{\pi}\frac{\partial\tan\left(\frac{\pi}{2}D_{\eta}\right)}{\partial D_{\eta}}\right]\Delta D_{\eta} \\ &+\frac{1}{2}k_{\eta}^{t}\left(B_{\eta}^{t}\right)^{2}H\left(u_{\eta}\right)\frac{\partial}{\partial D_{\eta}}\left[\left(D_{\eta}-1\right)\left(2-2\log\left(1-D_{\eta}\right)+\left(\log\left(1-D_{\eta}\right)\right)^{2}\right)\right]\Delta D_{\eta} \\ &\frac{1}{2}k_{\tau}u_{\tau}^{2}\Delta D_{\tau} \\ &+\frac{1}{2}k_{\tau}B_{\tau}^{2}\frac{\partial}{\partial D_{\tau}}\left[\left(D_{\tau}-1\right)\left(2-2\log\left(1-D_{\tau}\right)+\left(\log\left(1-D_{\tau}\right)\right)^{2}\right)\right]\Delta D_{\tau} \end{split}$$

and

$$\begin{split} &\langle \mathcal{E}'\left(u_{\eta},u_{\tau},D_{\eta},D_{\tau}\right),\left(\delta u_{\eta},\delta u_{\tau},\delta D_{\eta},\delta D_{\tau}\right)\rangle = \\ &= \int\limits_{t_{i}}^{t_{f}} \left\{k_{\eta}\left(1-D_{\eta}\right)u_{\eta} + k_{\tau}B_{\tau}\frac{\partial \widetilde{B}_{\tau}}{\partial u_{\eta}}\int\limits_{0}^{D_{\tau}}\left[Log\left(1-x\right)\right]^{2}dx - F_{\eta}^{ext}\right\}\delta u_{\eta} \\ &+ \left\{k_{\tau}\left(1-D_{\tau}\right)u_{\tau} - F_{\tau}^{ext}\right\} \cdot \delta u_{\tau} \\ &- \frac{1}{2}k_{\eta}u_{\eta}^{2}\delta D_{\eta} \\ &+ \frac{1}{2}k_{\eta}^{c}\left(B_{\eta}^{c}\right)^{2}H\left(-u_{\eta}\right)\left[-1 + \frac{2}{\pi}\frac{\partial\tan\left(\frac{\pi}{2}D_{\eta}\right)}{\partial D_{\eta}}\right]\delta D_{\eta} \\ &+ \frac{1}{2}k_{\eta}^{t}\left(B_{\eta}^{t}\right)^{2}H\left(u_{\eta}\right)\frac{\partial}{\partial D_{\eta}}\left[\left(D_{\eta}-1\right)\left(2-2\log\left(1-D_{\eta}\right) + \left(\log\left(1-D_{\eta}\right)\right)^{2}\right)\right]\delta D_{\eta} \\ &\frac{1}{2}k_{\tau}u_{\tau}^{2}\delta D_{\tau} \\ &+ \frac{1}{2}k_{\tau}B_{\tau}^{2}\frac{\partial}{\partial D_{\tau}}\left[\left(D_{\tau}-1\right)\left(2-2\log\left(1-D_{\tau}\right) + \left(\log\left(1-D_{\tau}\right)\right)^{2}\right)\right]\delta D_{\tau} \end{split}$$

where

$$\int_{0}^{D_{\tau}} \left[ Log (1-x) \right]^{2} dx = 2 + (D_{\tau} - 1) \left( 2 - 2 \log (1 - D_{\tau}) + (\log (1 - D_{\tau}))^{2} \right).$$

By assuming

$$(\delta u_{\eta}, \delta u_{\tau}, \delta D_{\eta}, \delta D_{\tau}) = (\Delta u_{\eta} + u, \Delta u_{\tau}, \Delta D_{\eta}, \Delta D_{\tau})$$

and then

$$(\delta u_{\eta}, \delta u_{\tau}, \delta D_{\eta}, \delta D_{\tau}) = (\Delta u_{\eta} - u, \Delta u_{\tau}, \Delta D_{\eta}, \Delta D_{\tau})$$

for arbitrary scalar u, we obtain two inequalities, that imply the following Euler-Lagrange equation for the normal displacement,

$$\left\{ -k_{\eta} \left( 1 - D_{\eta} \right) u_{\eta} - k_{\tau} B_{\tau} \frac{\partial \widetilde{B}_{\tau}}{\partial u_{\eta}} \int_{0}^{D_{\tau}} \left[ \log \left( 1 - x \right) \right]^{2} dx + F_{\eta}^{ext} \right\} \delta u_{\eta} = 0.$$

By assuming

$$(\delta u_{\eta}, \delta u_{\tau}, \delta D_{\eta}, \delta D_{\tau}) = (\Delta u_{\eta}, \Delta u_{\tau} + w, \Delta D_{\eta}, \Delta D_{\tau})$$

and then

$$(\delta u_{\eta}, \delta u_{\tau}, \delta D_{\eta}, \delta D_{\tau}) = (\Delta u_{\eta}, \Delta u_{\tau} - w, \Delta D_{\eta}, \Delta D_{\tau})$$

for arbitrary vector w, we obtain another set of two vector inequalities (two for each component), that imply another Euler-Lagrange equation for the tangential displacement,

$$\left\{ -k_{\tau} \left( 1 - D_{\tau} \right) u_{\tau} + F_{\tau}^{ext} \right\} \cdot \delta u_{\tau} = 0.$$

Besides, the variation of the irreversible kinematical quantities are not arbitrary but only positive. Thus, by assuming

$$(\delta u_{\eta}, \delta u_{\tau}, \delta D_{\eta}, \delta D_{\tau}) = (\Delta u_{\eta}, \Delta u_{\tau}, 2\Delta D_{\eta}, \Delta D_{\tau})$$

and then

$$(\delta u_{\eta}, \delta u_{\tau}, \delta D_{\eta}, \delta D_{\tau}) = (\Delta u_{\eta}, \Delta u_{\tau}, 0, \Delta D_{\tau})$$

we obtain another set of two inequalities, that imply another Euler-Lagrange equation for the normal damage in the form of the following KKT condition,

$$\left[u_{\eta}^{2} - \left(B_{\eta}^{t}\right)^{2} H\left(u_{\eta}\right) \left(\log\left(1 - D_{\eta}\right)\right)^{2} - \left(B_{\eta}^{c}\right)^{2} H\left(-u_{\eta}\right) \left[\tan\left(\frac{\pi}{2}D_{\eta}\right)\right]^{2}\right] \Delta D_{\eta} = 0.$$
 (54)

It is worth to be noted that, in the loading conditions (i.e. when  $\Delta D_{\eta} > 0$ ), the previous KKT condition is, in tension  $(u_{\eta} > 0)$ ,

$$u_{\eta} = -B_{\eta}^{t} \log \left(1 - D_{\eta}\right) \quad \Rightarrow \quad D_{\eta} = 1 - \exp\left(-\frac{u_{\eta}}{B_{\eta}^{t}}\right),$$
 (55)

and, in compression  $(u_{\eta} < 0)$ ,

$$u_{\eta} = -B_{\eta}^{c} \left[ \tan \left( \frac{\pi}{2} D_{\eta} \right) \right] \quad \Rightarrow \quad D_{\eta} = \frac{2}{\pi} \arctan \left( -\frac{u_{\eta}}{B_{\eta}^{c}} \right).$$
 (56)

By assuming

$$(\delta u_n, \delta u_\tau, \delta D_n, \delta D_\tau) = (\Delta u_n, \Delta u_\tau, \Delta D_n, 2\Delta D_\tau)$$

and then

$$(\delta u_{\eta}, \delta u_{\tau}, \delta D_{\eta}, \delta D_{\tau}) = (\Delta u_{\eta}, \Delta u_{\tau}, \Delta D_{\eta}, 0)$$

we obtain another set of two inequalities, that imply another Euler-Lagrange equation for the tangential damage in the form of the following KKT condition,

$$\left[u_{\tau}^{2} - B_{\tau}^{2} \left(\log\left(1 - D_{\tau}\right)\right)^{2}\right] \Delta D_{\tau} = 0.$$
 (57)

It is worth to be noted that, in the loading conditions (i.e. when  $\Delta D_{\tau} > 0$ ), the previous KKT condition is,

$$|u_{\tau}| = -B_{\tau} \log \left(1 - D_{\tau}\right) \quad \Rightarrow \quad D_{\tau} = 1 - \exp\left(-\frac{|u_{\tau}|}{B_{\tau}}\right),\tag{58}$$

#### 6 Results

We elucidate the properties of the model through analytical and numerical results presented for selected test cases. Two square specimens in 2D, with side S=10 [cm] (Fig. 2), are subjected to extension, compression and shearing tests, as sketched in Fig. 3, the quantity  $\bar{u}$  in Fig. 3 increasing from 0 to  $\bar{u}_{max}$ . The first specimen, without flaw, is designed to illustrate the model performance in the case of homogeneous deformation while the second, with a circular flaw (hole), for the case of inhomogeneous deformation under the same set of kinematic boundary conditions.

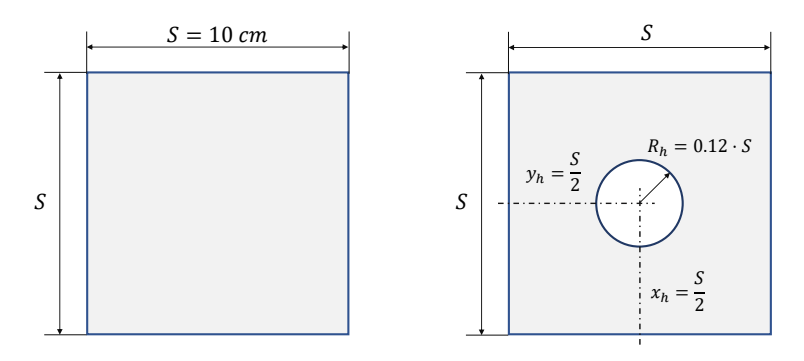


Figure 2: Schematics of analyzed domains, without (left-hand side) and with (right-hand side) the hole.

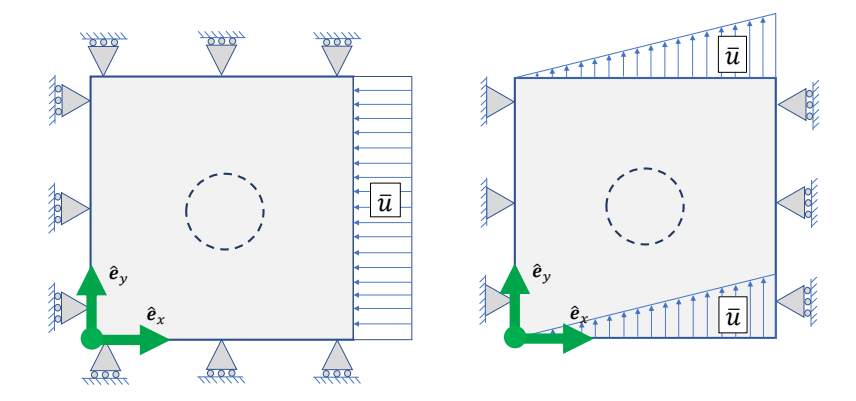


Figure 3: Schematics of considered boundary conditions. Extension (i.e.,  $\bar{u} < 0$ )/compression (i.e.,  $\bar{u} > 0$ ) test (left) and shearing test (right).

#### 6.1 Homogeneous deformations

It can be easily seen that, when a flawless (i.e. no hole) specimen is considered, then boundary conditions in Fig. 3 imply homogeneous deformations. Thus, strain gradient terms in the deformation energy are not activated, i.e.  $\nabla G = 0$ . For such boundary conditions, closed form solutions are available and will be analyzed in what follows. At first, let us define the displacement function  $\mathbf{u}(X) := \chi(X) - X$ . Component-wise, in the unit orthonormal basis  $(\hat{\mathbf{e}}_x, \hat{\mathbf{e}}_y)$  in Fig. 3, we have  $\mathbf{u}(X) = (u_1(X), u_2(X))$ , where  $X = (X_1, X_2)$ . In such a component-form, boundary conditions in Fig. 3 can be written as

• extension/compression test

$$u_1(0, X_2) = 0 \ \forall X_2 \in [0, S] \tag{59}$$

$$u_2(X_1, S) = 0 \ \forall X_1 \in [0, S] \tag{60}$$

$$u_2(X_1, 0) = 0 \ \forall X_1 \in [0, S] \tag{61}$$

$$u_1(S, X_2) = \bar{u} \ \forall X_2 \in [0, S]$$
 (62)

• shearing test

$$u_1(0, X_2) = 0 \ \forall X_2 \in [0, S] \tag{63}$$

$$u_2(0, X_2) = 0 \ \forall X_2 \in [0, S] \tag{64}$$

$$u_1(X_1, S) = 0 \ \forall X_1 \in [0, S] \tag{65}$$

$$u_1(X_1, S) = 0 \ \forall X_1 \in [0, S]$$
 (66)

$$u_1(X_1, 0) = 0 \ \forall X_1 \in [0, S] \tag{67}$$

$$u_1(S, X_2) = 0 \ \forall X_2 \in [0, S]$$
(68)

$$u_2(X_1, S) = \frac{\bar{u}}{S} \cdot X_1 \ \forall X_1 \in [0, S]$$
 (69)

$$u_2(X_1, 0) = \frac{\bar{u}}{S} \cdot X_1 \ \forall X_1 \in [0, S]$$
 (70)

$$u_2(S, X_2) = \frac{\bar{u}}{S} \cdot X_1 \ \forall X_2 \in [0, S]$$
 (71)

leading to the following solutions

• Extension/compression test. The displacement field is analytically given by the following expressions for its components,

$$u_1(X_1, X_2) = -\frac{\bar{u}}{S}X_1, \qquad u_2(X_1, X_2) = 0, \qquad \forall X_1 \in [0, S] \qquad \forall X_2 \in [0, S],$$

and, from (5), the Green-Saint-Venant tensor is found in terms of its matrix representation with respect to the given frame of reference,

$$G = \begin{pmatrix} \frac{\bar{u}}{S} \left( -1 + \frac{\bar{u}}{2S} \right) & 0\\ 0 & 0 \end{pmatrix}, \tag{72}$$

as well as the normal and the squared tangent displacement (10) and (14),

$$u_{\eta} = 2\bar{u}L\left(-1 + \frac{\bar{u}}{2S}\right)\cos^2(\theta),\tag{73}$$

$$u_{\tau}^{2} = \left[2\bar{u}L\left(-1 + \frac{\bar{u}}{2S}\right)\cos(\theta)\sin(\theta)\right]^{2}.$$
 (74)

• Shearing test. The displacement field is analytically given by the following expressions for its components,

$$u_1(X_1, X_2) = 0,$$
  $u_2(X_1, X_2) = \frac{\bar{u}}{S} X_1,$   $\forall X_1 \in [0, S]$   $\forall X_2 \in [0, S]$ 

and, from (5), the Green-Saint-Venant tensor is found in terms of its matrix representation with respect to the given frame of reference,

$$G = \begin{pmatrix} 0 & \frac{\bar{u}}{2S} \\ \frac{\bar{u}}{2S} & 0 \end{pmatrix}, \tag{75}$$

as well as the normal and squared tangent displacement (10) and (14),

$$u_{\eta} = 2\bar{u}\cos(\theta)\sin(\theta),\tag{76}$$

$$u_{\tau}^{2} = \bar{u}^{2} \left( 1 - 4\cos^{2}(\theta)\sin^{2}(\theta) \right). \tag{77}$$

It is worthwhile to remark that, as the resulting deformations are homogeneous, the relative displacements  $u_{\eta}$  and  $u_{\tau}$  do not depend on the position X but depend only on the angle  $\theta$ . Applying the KKT conditions in Eqs. (55, 56, 58), observing that each grain-pair of the micro-scale system is monotonically loaded (i.e.  $\Delta D_{\eta}(\theta)$ ,  $\Delta D_{\tau}(\theta)$  are strictly greater than zero for each  $\bar{u}$ ), we obtain an analytic expression of the damage variables

$$D_{\eta}(\theta) = \begin{cases} 1 - \exp\left(-\frac{u_{\eta}(\theta)}{B_{\eta}^{t}}\right), & u_{\eta}(\theta) > 0\\ \frac{2}{\pi}\arctan\left(-\frac{u_{\eta}(\theta)}{B_{\eta}^{c}}\right), & u_{\eta}(\theta) < 0 \end{cases}$$
(78)

and

$$D_{\tau}(\theta) = 1 - \exp\left(-\frac{|u_{\tau}(\theta)|}{B_{\tau}}\right) \tag{79}$$

which are plotted in Fig. 4 for the three boundary conditions. For the case of shear, certain grain-pair directions experience tensile loading (those in the interval  $\theta \in (0, \pi/2) \cup (\pi, 3\pi/2)$ ) while those in the interval  $\theta \in (\pi/2, \pi) \cup (3\pi/2, 2\pi)$  experience compression. Therefore, the petals of the flower-like plots for normal damage evolve differently, with those for tensile directions tending towards the direction 1 earlier than for compressive directions (for which the threshold for damage is higher).

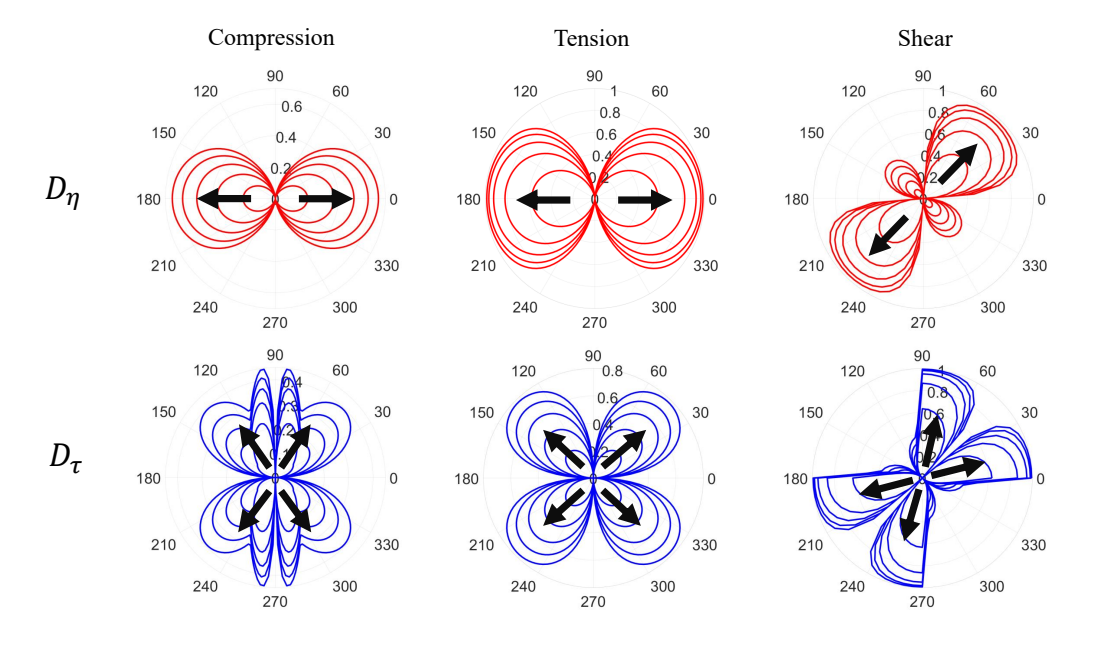


Figure 4: Polar plots of the damage variables  $D_{\eta}$  and  $D_{\tau}$  for different homogeneous test cases and for increasing  $\bar{u}$ . Black arrows indicate directions of increasing  $\bar{u}$ .

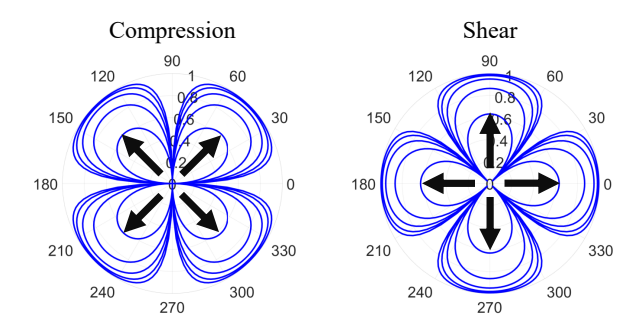


Figure 5: Polar plots of the damage variable  $D_{\tau}$  for homogeneous compression and shearing tests and for increasing  $\bar{u}$  when  $B_{\tau} = B_{\tau 0} = const$  is considered and therefore equation (48) is not taken into account. Black arrows indicate directions of increasing  $\bar{u}$ .

Further, the flower-like shape of tangential damage plots in Fig. 4 are distorted due to the non-smooth evolution of  $B_{\tau}$  according to Eq. (48) for grain-pair directions experiencing compressive actions or tensile versus compressive actions. To better elucidate this fact, Fig. 5 shows the tangential damage for compression and shearing test considering a constant dependence, i.e.  $B_{\tau} = B_{\tau 0}$ , for the characteristic length of the tangent damage dissipation.

The directional variation in the evolution of damage variables has two critical consequences that are of significance for correctly describing the behavior of materials that display tension-compression asymmetry and evolving anisotropy at the macro-scale. Firstly, the model is able to predict a stiffer and stronger behavior under compression as opposed to that under extension, that is coherent with observation relevant to a number of previously mentioned materials. Secondly, the model predicts an evolution of anisotropy as the material undergoes damage in preferred direction when a specimen in subjected to a specific boundary conditions. Examples of such materials abound in the literature. Here we mention a few material cases to underline the significance of the taken approach, for example soft biological tissue [45]; woods [48]; metals [46]; besides the widely known behavior of ceramics, geomaterials, and cementitious materials such as concrete.

With the aim to provide further insight into the meaning of the various parameters used within the modeling, a sensitivity analysis is presented for the simple homogeneous cases considered in this subsection. Particularly, we investigate how damage parameters affect the elastic response. In the case of homogeneous compression, the normal displacement  $u_{\eta}$  is always negative. It is for this reason that only the influence of 4 damage parameters out of 5 is to be investigated. Indeed, the characteristic length of tension dissipation  $B_n^t$  in Eq. (78) does not play any role in such a situation. For the homogeneous extension test we have something analogous: since  $u_{\eta}$  is always positive, the parameters  $B_n^c$ ,  $\alpha_1$ ,  $\alpha_2$  do not have any effect on the results. While, for the shearing test, every parameter is relevant. In Figs. 6-8, force-displacement diagrams are reported for compression, extension and shearing tests, each of them considering a single varying material parameter. It is observed that the specimen's softening in homogeneous compression decreases by augmenting the parameters  $B_n^c$  (Fig. 6(top-left)),  $B_{\tau 0}$  (Fig. 6(top-right)),  $\alpha_1$  (Fig. 6(bottom-left)), and  $\alpha_2$  (Fig. 6(bottom-right)). Analogously, for the homogeneous extension test, specimen's softening decreases by augmenting the parameters  $B_n^t$  (Fig. 7(left)) and  $B_{\tau 0}$  (Fig. 7(right)). Also for the shearing test it is observed that specimen's softening decreases by augmenting the parameters  $B_{\eta}^{c}$  (Fig. 8(top-left)),  $B_{\eta}^{t}$  (Fig. 8(top-right)),  $B_{\tau 0}$  (Fig. 8(center)),  $\alpha_1$  (Fig. 8(bottom-left)), and  $\alpha_2$  (Fig. 8(bottom-right)).

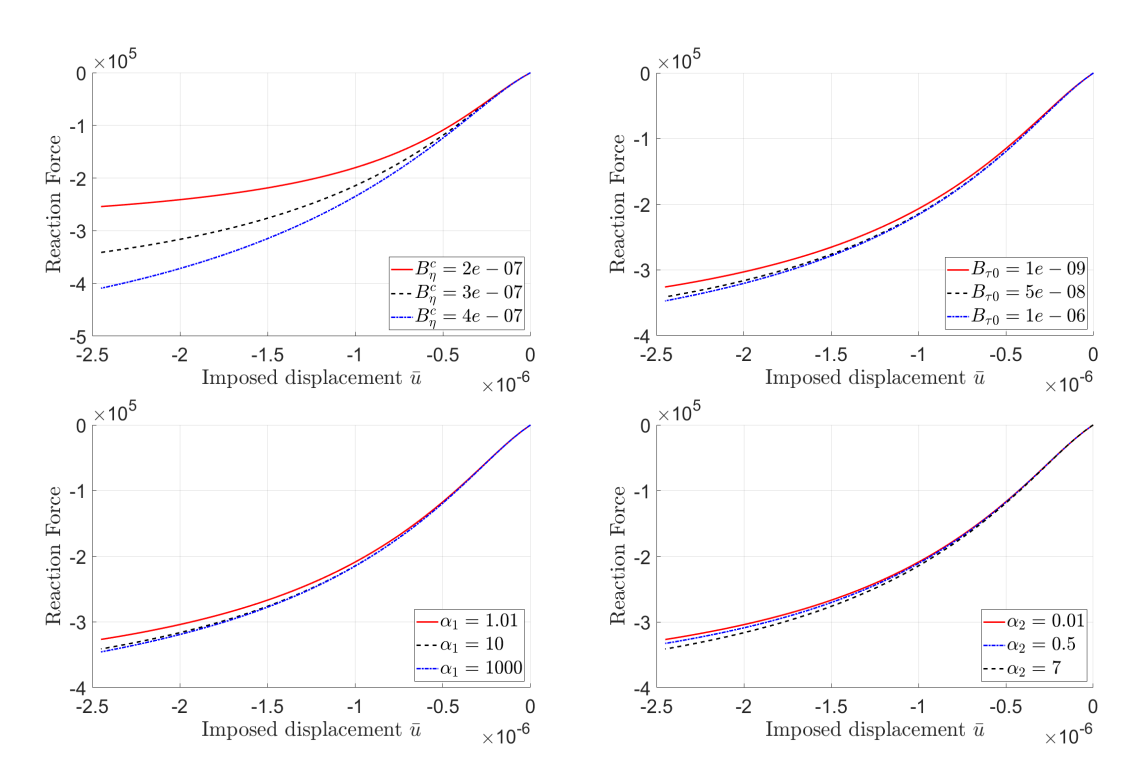


Figure 6: Sensitivity analysis. Force vs displacement diagrams for homogeneous compression test obtained by varying different model parameters, i.e.  $B_{\eta}^{c}$  (top-left),  $B_{\tau 0}$  (top-right),  $\alpha_{1}$  (bottom-left), and  $\alpha_{2}$  (bottom-right).

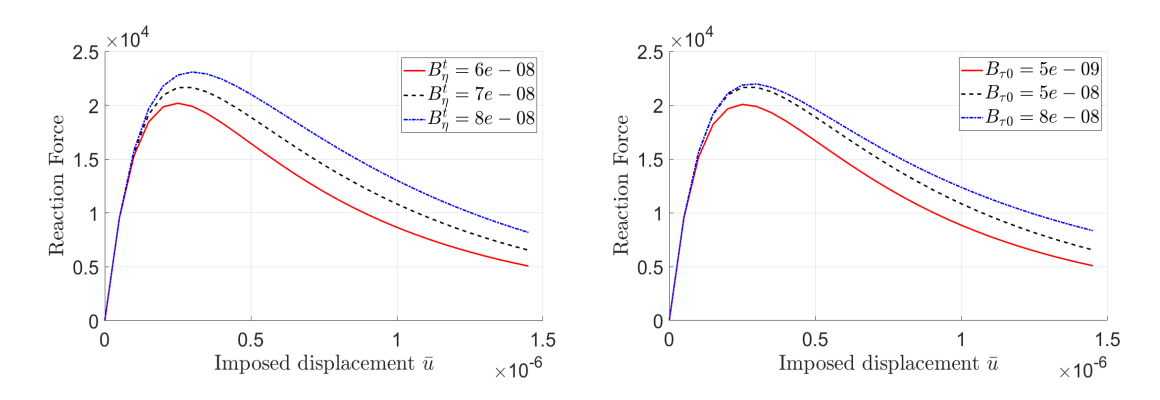


Figure 7: Sensitivity analysis. Force vs displacement diagrams for homogeneous extension test obtained by varying different model parameters, i.e.  $B_{\eta}^{t}$  and  $B_{\tau 0}$  (right).

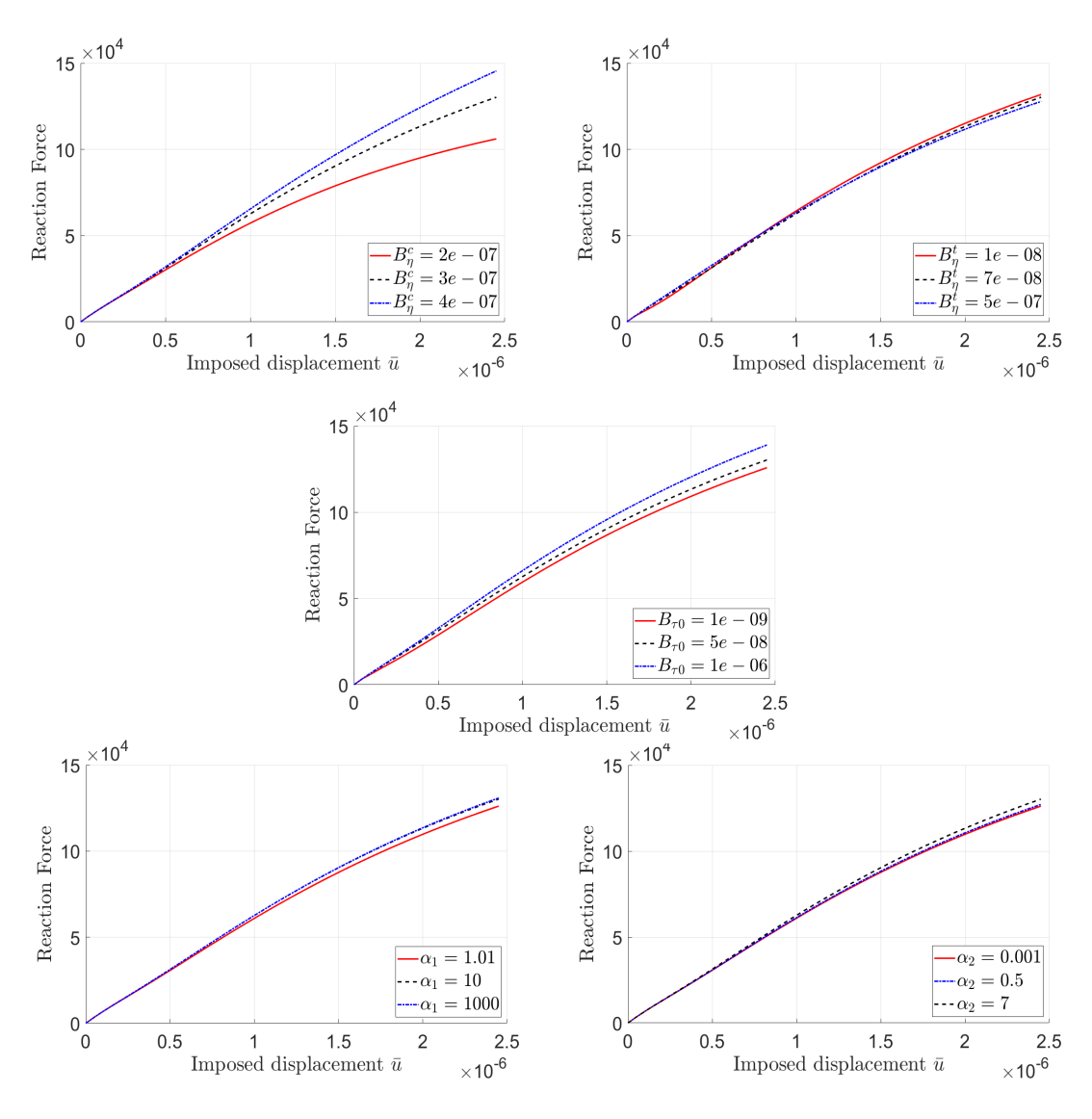


Figure 8: Sensitivity analysis. Force vs displacement diagrams for homogeneous shearing test obtained by varying different model parameters, i.e.  $B_{\eta}^{c}$  (top-left),  $B_{\eta}^{t}$  (top-right),  $B_{\tau 0}$  (center),  $\alpha_{1}$  (bottom-left), and  $\alpha_{2}$  (bottom-right).

#### 6.2 Implementation of the numerical algorithm

For the solution of problems that include non-homogeneous deformations, numerical effort is needed. To this end, an algorithm was developed for the numerical implementation of the model. To illustrate the model applicability, the algorithm was used to compute results for three exemplary cases, i.e. non-homogeneous extension/compression and shearing tests. The continuum model is solved by means of the commercial software Matlab and COMSOL Multiphysics. An iterative procedure is implemented in a staggered fashion in Matlab as described in the flowchart in Fig. 9, making use of COMSOL Multiphysics as a subroutine solving the elastic equilibrium problem.

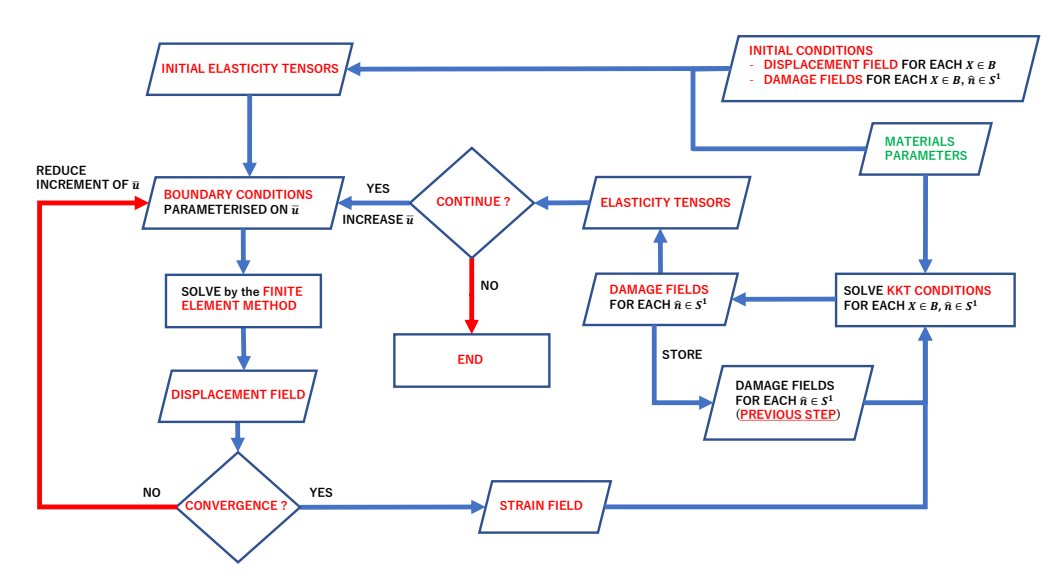


Figure 9: Flowchart of the numerical iterative procedure used to solve the mathematical formulation.

The steps of the iterative procedure can be resumed as follows:

- 1. null initial conditions on the displacement field u and damage fields  $D_{\eta}$  and  $D_{\tau}$  are given together with the material parameters  $L, k_{\eta}^c, k_{\eta}^t, k_{\tau}, B_{\eta}^c, B_{\eta}^t, B_{\tau 0}$ , according to Tab. 1. The stiffnesses  $k_{\eta}^c, k_{\eta}^t, k_{\tau}$  given as input material parameters may be initially isotropic, i.e. they do not need to depend on the orientation angle  $\theta$ . It is worth to mention that the effective (i.e. damaged-) stiffnesses  $k_{\eta,D}^c, k_{\eta,D}^t, k_{\tau,D}$  may change during the evolution of the system due to the damage induced by the state of deformation, thus leading to non-isotropically distributed effective (damaged-) stiffnesses. Indeed, owing to Eq. (19), this is the reason why for a given basis the components of the elasticity tensors may change during the evolution of the system, possibly implying anisotropy shifts;
- 2. the fourth-rank ( $\mathbb{C}_{ijab}$ ), the fifth-rank ( $\mathbb{M}_{ijabc}$ ) and the sixth-rank ( $\mathbb{D}_{ijhabc}$ ) elasticity tensors are computed according to Eqs. (28, 29 and 30). Such elastic tensors, as well as boundary conditions, are given as input to a finite element subroutine based on COMSOL Multiphysics. Particularly, the weak form of the equilibrium problem in Eq. (53) is solved by means of the weak form package. Quintic Argyris polynomials are used as shape functions ensuring  $C^2$  continuity across elements along the normal to element boundaries. A Delaunay-tessellated triangular mesh was employed. Different mesh sizes were considered to investigate mesh independence. The output of this subroutine is the displacement field;
- 3. the increment of the displacement field with respect to the previous step is node-wise compared with a tolerance. When such a tolerance is not respected, then the displacement parameter  $\bar{u}$  is reduced to re-initialize the finite element subroutine;
- 4. when the increment of the displacement field with respect to the previous step compares positively with the above-mentioned chosen tolerance, then the strain field G is computed making use of the displacement field. The strain field is then used by means of Eqs. (7-12) to compute the relative displacements  $u_{\eta}$ ,  $u_{\tau}$ , which depend on the space coordinates and on the angle  $\theta$ . Such

displacements are then given as input to the KKT conditions in Eqs. (55, 56, 58). The damage fields  $D_{\eta}$  and  $D_{\tau}$  are recovered as an output of KKT conditions. In formulas, we have

$$D_{\eta}^{t} = \max \left\{ D_{\eta}, D_{\eta}^{t-1} \right\}, \quad D_{\tau}^{t} = \max \left\{ D_{\tau}, D_{\tau}^{t-1} \right\}, \tag{80}$$

where t is an index used to label the loading steps. Please remark that, according to Eqs. (55, 56 and 58) damage fields cannot reach the unit value;

#### 5. the load parameter $\bar{u}$ is increased.

The instructions above (from point 2) are repeated until a termination criterion is not verified. As mentioned at the beginning of the section, the termination criterion is given by  $\bar{u}$  reaching a maximum desired value  $\bar{u}_{max}$ . In order to smooth the constitutive assumption in Eq. (20), the Heaviside function H(x) is replaced by the following smooth function [70]

$$\frac{1}{2} + \frac{1}{\pi}\arctan\left(\frac{x}{\alpha}\right) \tag{81}$$

so that the non-damaged normal stiffness is defined as a smooth function of the normal relative displacement

$$k_{\eta} = \frac{1}{2} \left( k_{\eta}^t + k_{\eta}^c \right) + \frac{1}{\pi} \left( k_{\eta}^t - k_{\eta}^c \right) \arctan \left( \frac{u_{\eta}}{\alpha} \right), \tag{82}$$

that in turns gives the damaged normal stiffness as a smooth function of the normal relative displacement

$$k_{\eta,D} = \frac{1}{2} \left( k_{\eta}^t + k_{\eta}^c \right) (1 - D_{\eta}) + \frac{1}{\pi} \left( k_{\eta}^t - k_{\eta}^c \right) \arctan\left( \frac{u_{\eta}}{\alpha} \right) (1 - D_{\eta}). \tag{83}$$

The quantity  $\alpha$  can be tuned to modulate the regularization. Large values of  $\alpha$  enhance the convergence of the algorithm. A value for  $\alpha$  is considered, see Tab. 1, as to give a sufficiently smooth and non-stiff problem while not being detrimental to the congruence of Eqs. (20, 82) and Eqs. (21, 83), so that the physical meaning of  $\alpha$  can be overlooked.

L[m]	$k_{\eta}^{c}[J/m^{4}]$	$k_{\eta}^t [J/m^4]$	$k_{\tau}[J/m^4]$	$B_{\eta}^{c}[\mathrm{m}]$	$B_{\eta}^{t}[\mathrm{m}]$	$B_{\tau}[\mathrm{m}]$	$\alpha_1[1]$	$\alpha_2[1]$	$\alpha[1]$
0.01	$3.5 \cdot 10^{14}$	$3.5 \cdot 10^{13}$	$3 \cdot 10^{13}$	$3 \cdot 10^{-7}$	$7 \cdot 10^{-8}$	$5 \cdot 10^{-8}$	10	7	$5 \cdot 10^{-8}$

Table 1: Values of parameters used in numerical tests. Different parameters are used in the sequel for sensitivity analyses. Their values are reported in the corresponding plots.

#### 6.3 Non-homogeneous deformations

We further discuss the results for non-homogeneous extension, compression and shearing tests of a square domain with circular hole exemplified in Fig. 2(right). Since the solutions to the related elastic problem are not available in closed form, and observing that not all grain-pair (springs of the micro-scale system) might be monotonically loaded (i.e.  $\Delta D_{\eta}(\theta)$  and  $\Delta D_{\tau}(\theta)$  are not necessarely strictly greater than zero for each  $\bar{u}$ ), the iterative numerical solution strategy described in the previous subsection has been employed. Numerical values for the number of nodes  $N_{\theta}$  used to discretize the integration interval  $[0,2\pi]$  in Eq. (24), for the interval  $[\bar{u}_{min},\bar{u}_{max}]$  and for the number of converged load steps  $N_{iter}$  are provided in Table 2 for the three non-homogeneous tests. Fig. 10 presents a convergence analysis with respect to the maximum mesh element size in the case of the non-homogeneous extension test. It is observed that for the initial linear and softening phases all meshes give almost overlapping results in terms of global elastic response, i.e. total reaction force vs prescribed displacement. Progressively, for increasing prescribed displacement, an increasingly relevant mesh dependency is observed, most likely due to propagation of errors and to the increasing non-linearity and ill-posedness (damage is increasing thus leading to some vanishing first gradient, mixed first-second gradient, and second gradient elastic coefficients) of the elastic problem. Notwithstanding these phenomena, according to Fig. 10, superlinear convergence with respect to the mesh size in terms of global elastic response holds.

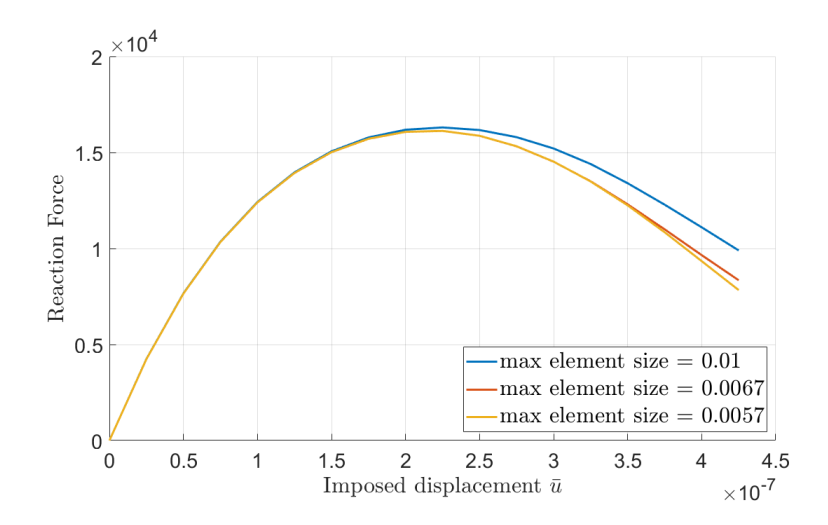


Figure 10: Mesh-convergence analysis. Global elastic response, i.e. total reaction force vs prescribed displacement, for different maximum mesh element sizes in the case of the non-homogeneous extension test. Element sizes in the legend are expressed in meters.

$N_{ heta}$	${ m compression/shear}$			tension			
	$N_{iter}$	$\Delta \bar{u}[\mathrm{m}]$	$\bar{u}_{max}[\mathrm{m}]$	$N_{iter}$	$\Delta \bar{u}[\mathrm{m}]$	$\bar{u}_{max}[\mathrm{m}]$	
120	50	$5 \cdot 10^{-8}$	$25 \cdot 10^{-7}$	16	$2.5 \cdot 10^{-8}$	$4 \cdot 10^{-7}$	

Table 2: Numerical values used in numerical simulations for non-homogeneous tests.

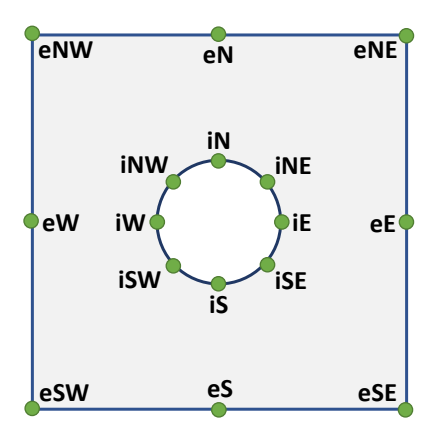


Figure 11: Legend of points referred to in subsequent damage polar plots. Nomenclature of the points is as follows. The first letter refers to internal (i) or external (e) points. Second and eventual third letter refer to geographic directions, i.e. N is for north, NE is for north-east, E is for east, SE is for South-east, S is for south, SW is for south-west, W is for west and NW is for north-west.

For all the subsequent simulations, the finest mesh was chosen. Needless to say, the presence of circular hole leads to a non-homogeneous deformation that localizes resulting in eventual failure of the specimen that can be perceived as zones in which damage parameters tend to unity. What is most significant about the current model is that the non-homogeneous deformation has implication at the underlying micro- or the grain-scale behavior of the continua. The consequence is that every point in the continuum body is not only in a different state from the viewpoint of continuum variables but also at a different state at the micro-scale. Thus at every point of the continuum body, different phenomena emerge and evolve as the loading progresses. For example, at certain locations in the body, an erstwhile isotropic and non-chiral material transforms into anisotropic material with chirality. These emergent behavior is best illustrated by following the evolution of damage parameters at the micro-scale by considering its direction distribution at selected points in the body as well as the evolution of its maximum value in

the body. Figs. 12, 16, and 20 show the evolution of  $D_{\eta}(\theta)$  at different points of the specimen (see the legend in Fig. 11) for the non-homogeneous compression, shearing, and extension tests, respectively. Figs. 14, 18, and 22 show the evolution of  $D_{\tau}(\theta)$  at different points of the specimen (see the legend in Fig. 11) for the non-homogeneous compression, shearing, and extension tests, respectively. Figs. 13, 17, and 21 show the contour plot of the maximum  $D_{\eta}(\theta)$  over  $\theta \in [0, 2\pi]$  for increasing loading steps. Finally, Figs. 15, 19, and 23 show the contour plot of the maximum  $D_{\tau}(\theta)$  over  $\theta \in [0, 2\pi]$  for increasing loading steps.

We remark that, owing to boundary conditions and domain symmetries, many connections can be traced among polar plots of the same damage variable at different domain points and within a single polar plot. For instance, the polar plots of  $D_{\eta}(\theta)$  at points "iS", "iNE" and "iSW" are obtained by reflecting with respect to the line  $\theta=0^{\circ}$  the polar plots of  $D_{\eta}(\theta)$  at points "iN", "iSE" and "iNW", respectively. The polar plots of  $D_{\eta}(\theta)$  at points "iE", "iNE", and "iSE" are obtained by reflecting with respect to the line  $\theta=90^{\circ}$  the polar plots of  $D_{\eta}(\theta)$  at points "iW", "iNW", and "iSW", respectively. The polar plots of  $D_{\eta}(\theta)$  at points "eS", "eSW", "eW", and "eNE" are the same of those at points "eN", "eNW", "eE", and "eSE", respectively. Analogous symmetries can be observed for the subsequent damage polar plots. We further note that, if  $G_{ij,k}=0$ , then, according to Eqs. (9, 14),  $u_{\eta}(\theta)=u_{\eta}(\theta+180^{\circ})$  and  $u_{\tau}(\theta)=u_{\tau}(\theta+180^{\circ})$ , the same symmetry thus holding for the damage variables. Clearly, this is verified for the homogeneous tests. For the non-homogeneous tests, the deviation from this symmetry condition is as much more evident as the strain gradient is relevant in magnitude (see the points "iS", "iSW", "iW", "iNW", "iN", "iNE", "iE", and "iSE", i.e. in the internal hole boundary). As we will better comment in the following, this leads to an induced non-centro-symmetric (i.e., chiral) behavior of the macroscopic agglomerate.

For compression test, it is interesting to observe from Figs. 12 and 14 that the presence of circular hole results in development of tensile damage at the corner points "eSW", "eNW", "eNE" and "eSE", in addition to the points at the perimeter of the hole. Furthermore, damage evolution remains centrosymmetric at the corner and outer-edge locations indicating that these points are unaffected by the strain gradients as in Figs. 12 and 14. On the other hand, at the points on the hole perimeter significant strain-gradients develop, leading to different grain-pair relative displacements for  $\theta$  and  $\theta+\pi$ directions predicted by Eq. (9). As a result, the damage evolution becomes non-centro-symmetric. The consequence is that the elastic moduli predicted by Eqs. (28), (29) and (30) becomes not only anisotropic but also chiral of different degrees. For the shear test, damage evolution remains centrosymmetric only at the outer-edge locations while the corner points become increasingly non-centrosymmetric as seen in Figs. 16 and 18. Clearly, the damage evolution is highly complex which is reflected in the mixed mode by which the micro-scale failure evolves as seen in 17 and 19. Finally for the case of extension test, the damage evolution shares the spatial similarity to the compression test for the selected points with the exception that all grain-pair directions experience extension as seen from Figs. 20 and 22. In this case, micro-separations due to grain-pair extension dominates, and as expected, the specimen develops a fracture initiating at the hole perimeter and progressing towards the outer edge perpendicular to the loading direction as seen in Figs. 21 and 23. Finally, we remark that an interpretation for the damage results of boundary points and for those angles indicating directions going out of the domain can be done only by taking into account that we are dealing with a continuous model and grain-pairs at the boundary are intended only close to the boundary.

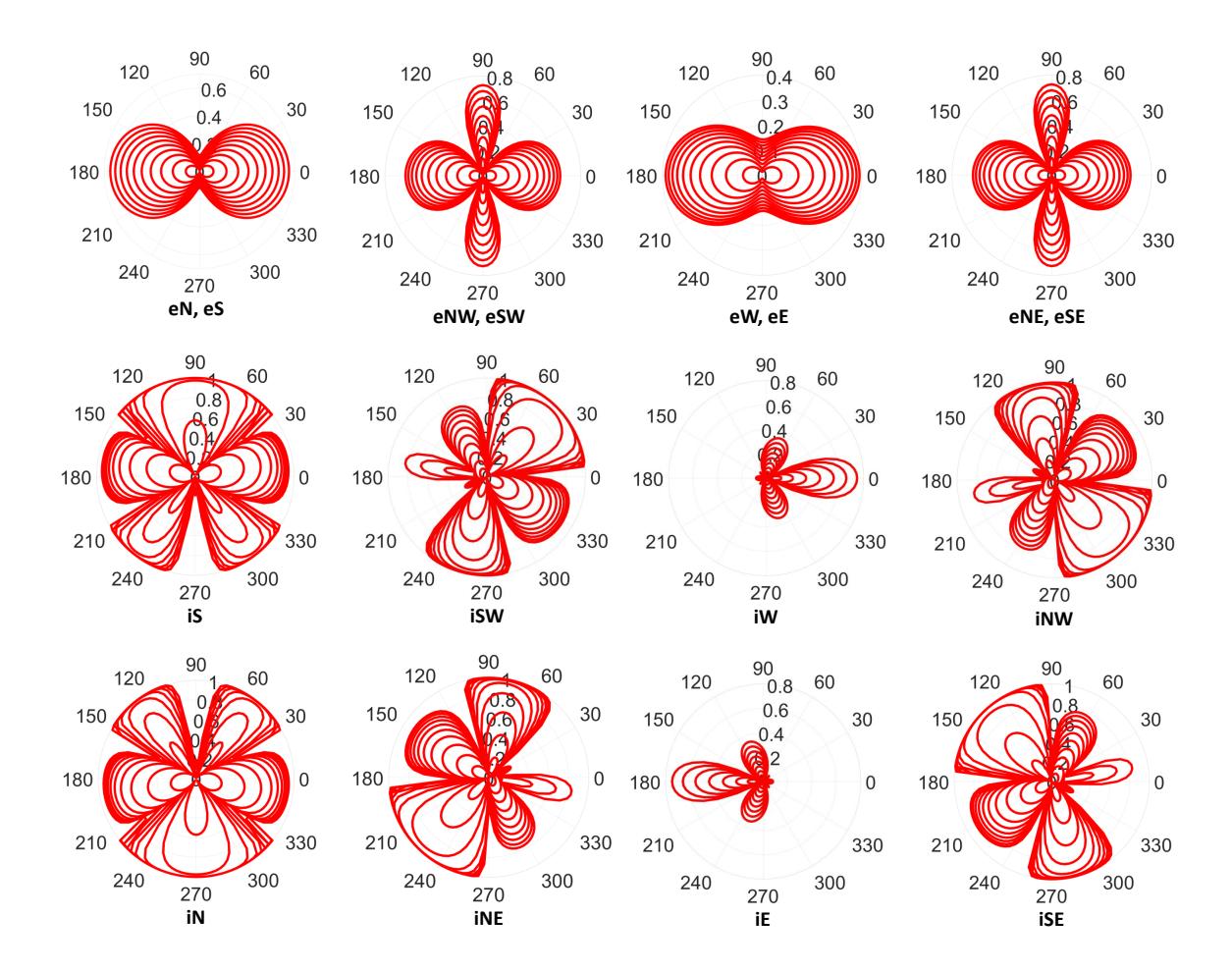


Figure 12: Non-homogeneous compression test. Evolution of  $D_{\eta}(\theta)$  at different points of the specimen (see the legend in Fig. 11).

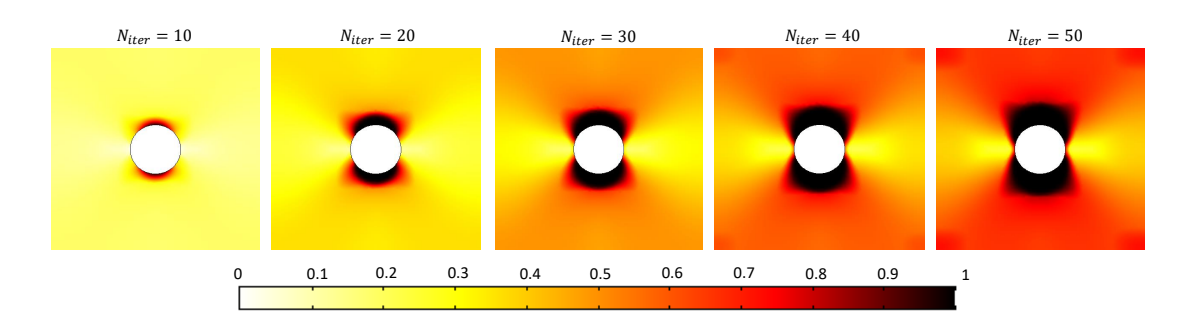


Figure 13: Non-homogeneous compression test. Contour plots of maximum  $D_{\eta}(\theta)$  over  $\theta \in [0, 2\pi]$  for increasing loading steps, showing the micro-scale damage evolution in the body modeled as a continuum which can be interpreted as micro-separations for grain-pair extension or crushing under grain-pair compression. Clearly around the hole perimeter, the micro-separations and crushing develops the loading proceeds.

maximum  $D_{\eta}$ 

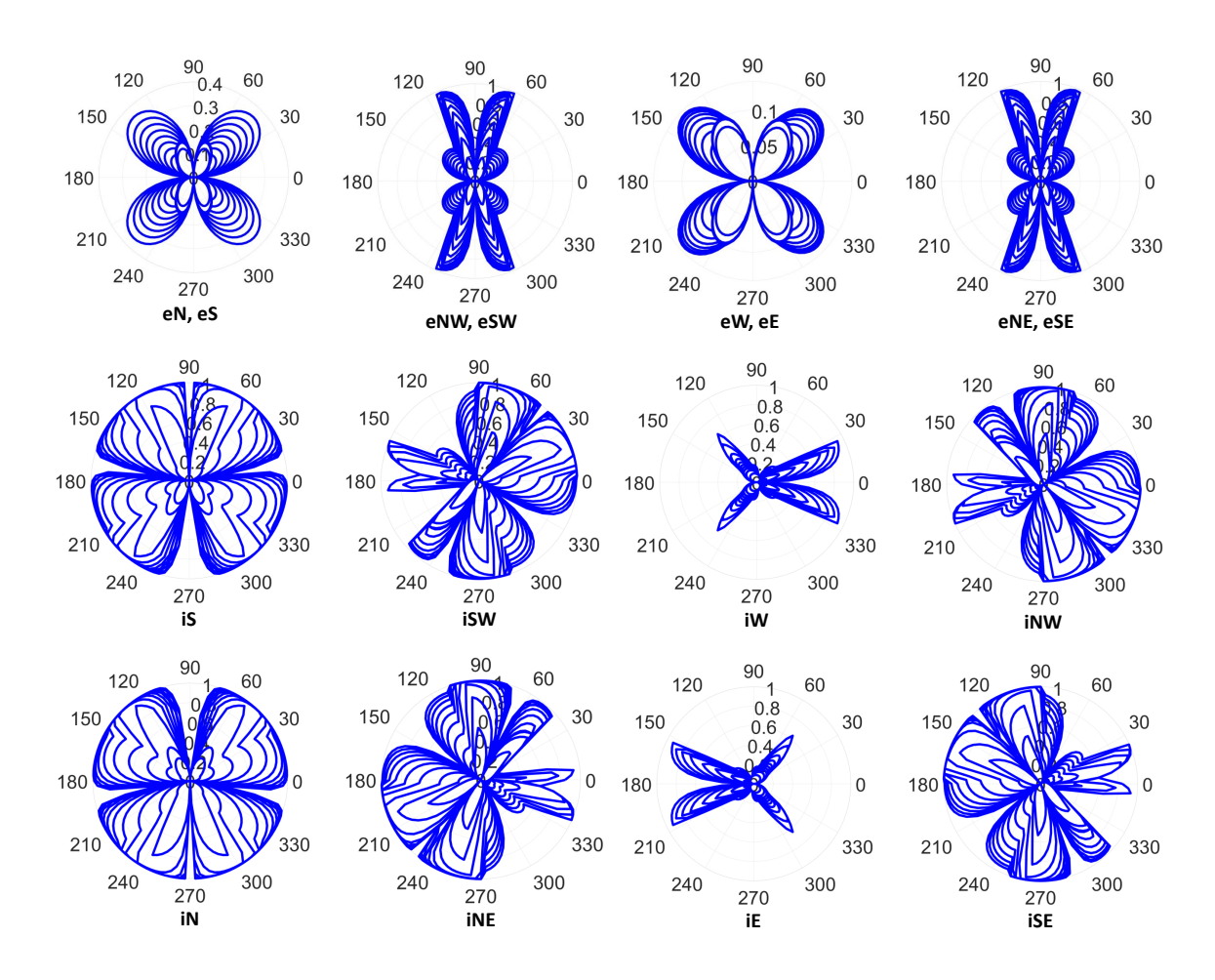


Figure 14: Non-homogeneous compression test. Evolution of  $D_{\tau}(\theta)$  at different points of the specimen (see the legend in Fig. 11).

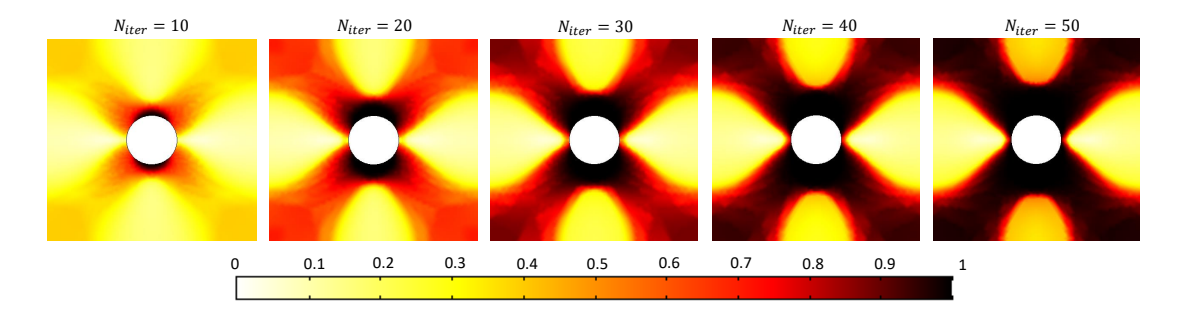


Figure 15: Non-homogeneous compression test. Contour plots of maximum  $D_{\tau}(\theta)$  over  $\theta \in [0, 2\pi]$  for increasing loading steps, showing the micro-scale damage evolution in the body modeled as a continuum. This damage evolution can be interpreted as grain-pair micro-shear. It is clear that under compression, micro-shear damage dominates leading to a shear localization at failure.

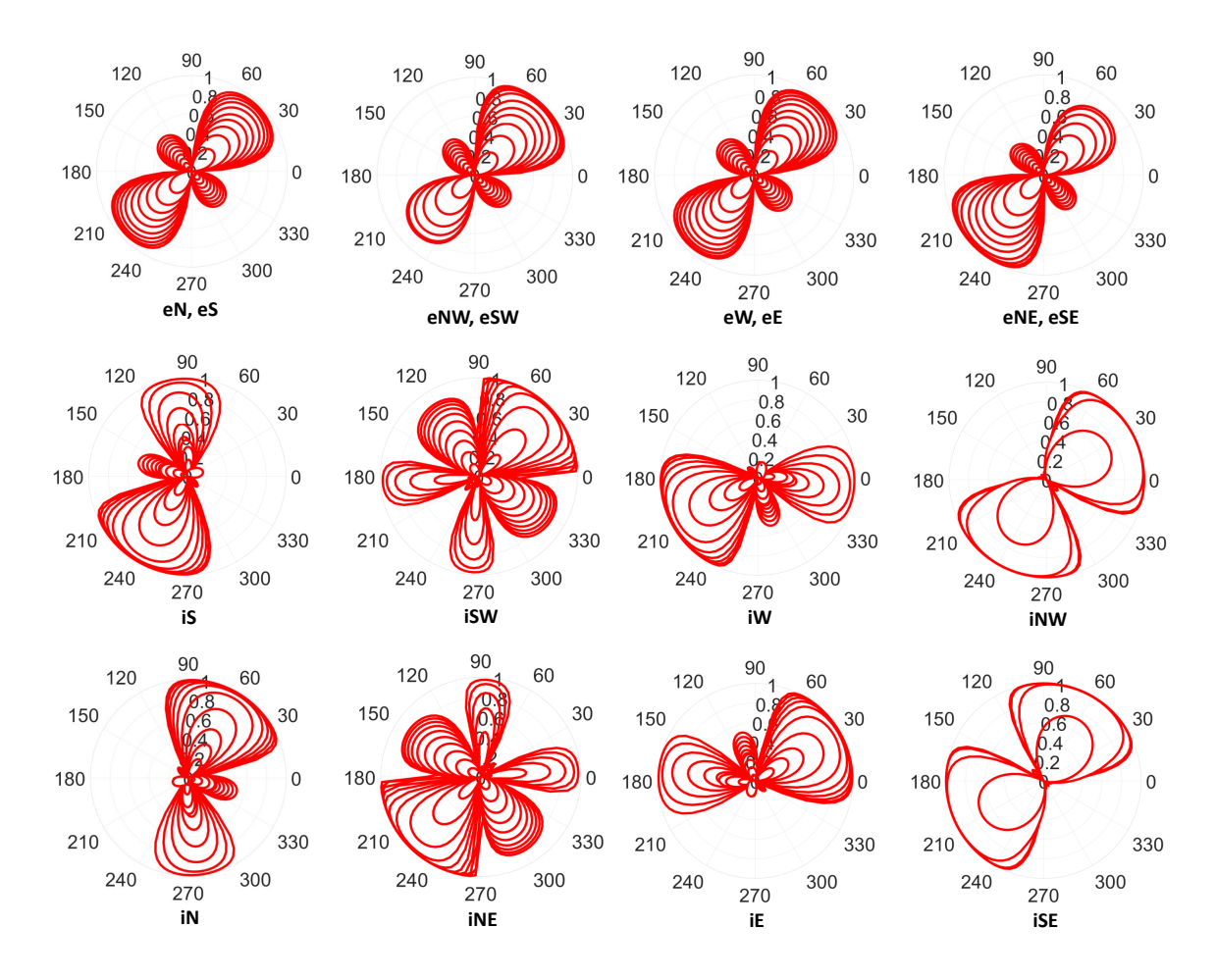


Figure 16: Non-homogeneous shearing test. Evolution of  $D_{\eta}(\theta)$  at different points of the specimen (see the legend in Fig. 11).

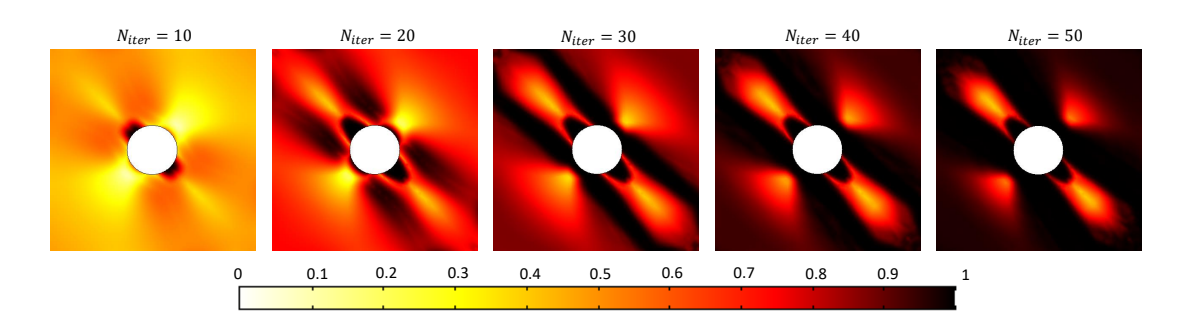


Figure 17: Non-homogeneous shearing test. Contour plots of maximum  $D_{\eta}(\theta)$  over  $\theta \in [0, 2\pi]$  for increasing loading steps.

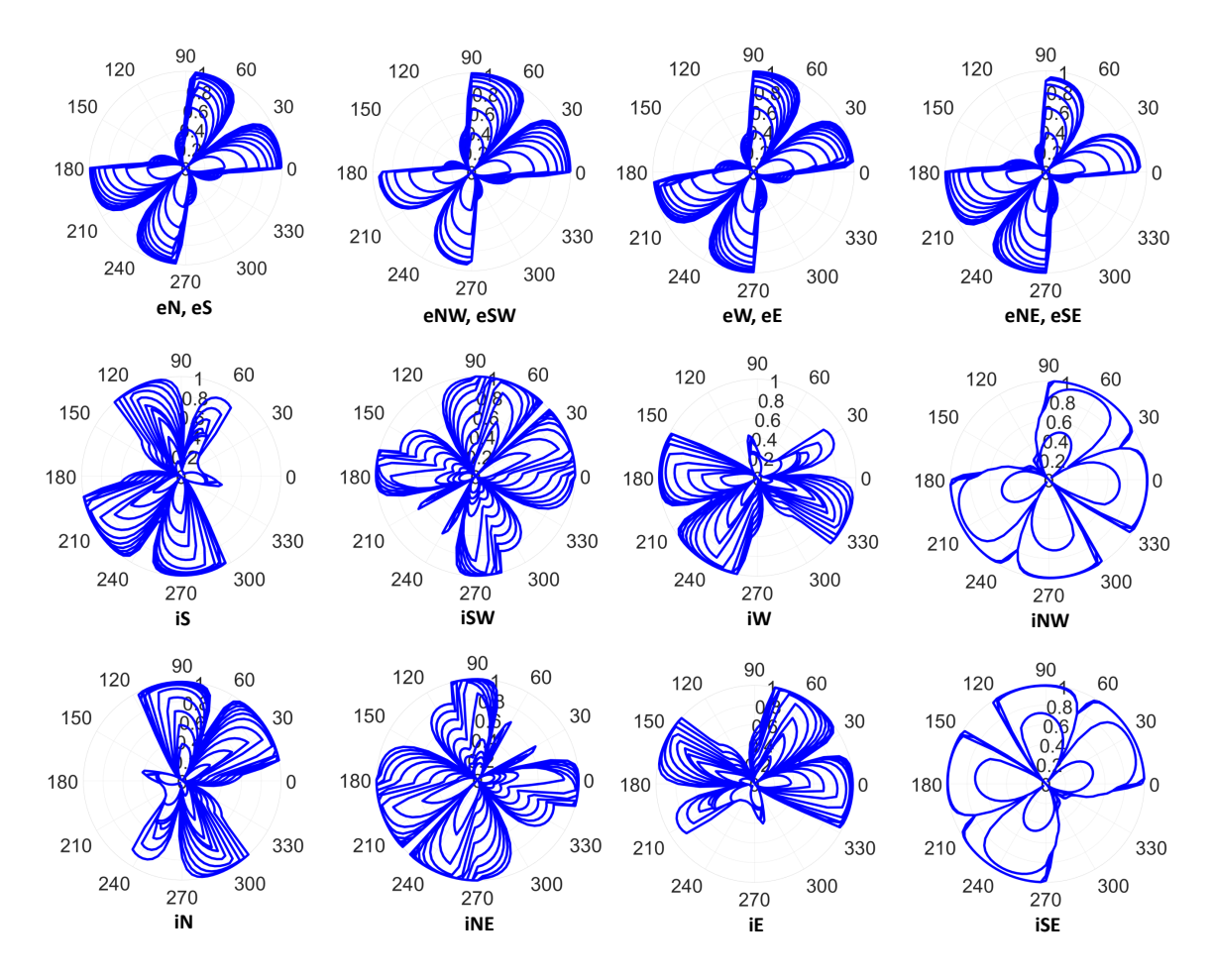


Figure 18: Non-homogeneous shearing test. Evolution of  $D_{\tau}(\theta)$  at different points of the specimen (see the legend in Fig. 11).

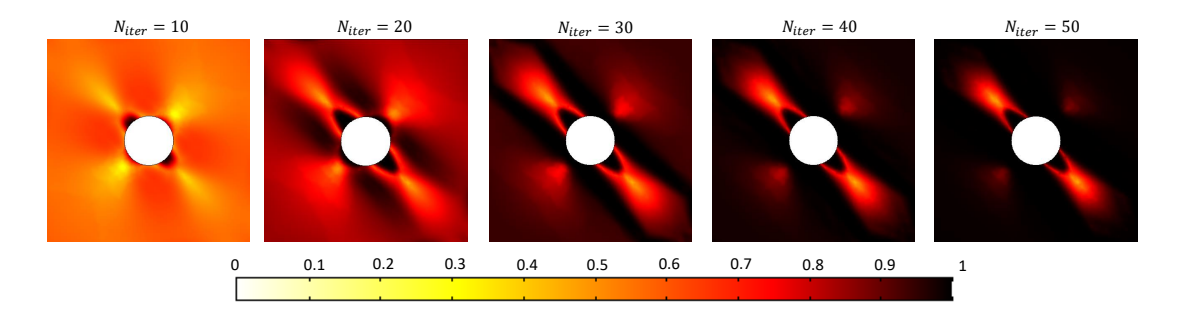


Figure 19: Non-homogeneous shearing test. Contour plots of maximum  $D_{\tau}(\theta)$  over  $\theta \in [0, 2\pi]$  for increasing loading steps.

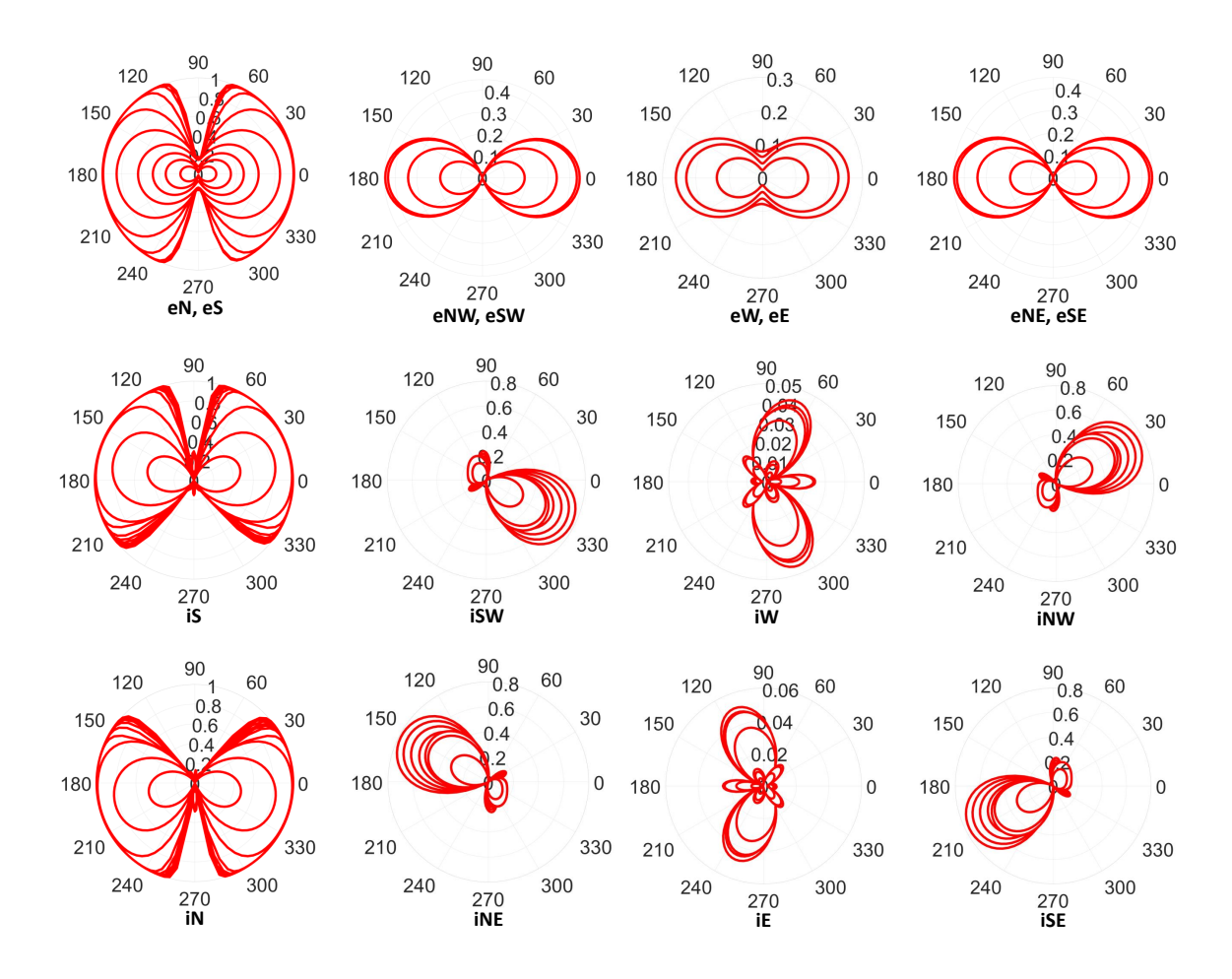


Figure 20: Non-homogeneous extension test. Evolution of  $D_{\eta}(\theta)$  at different points of the specimen (see the legend in Fig. 11).

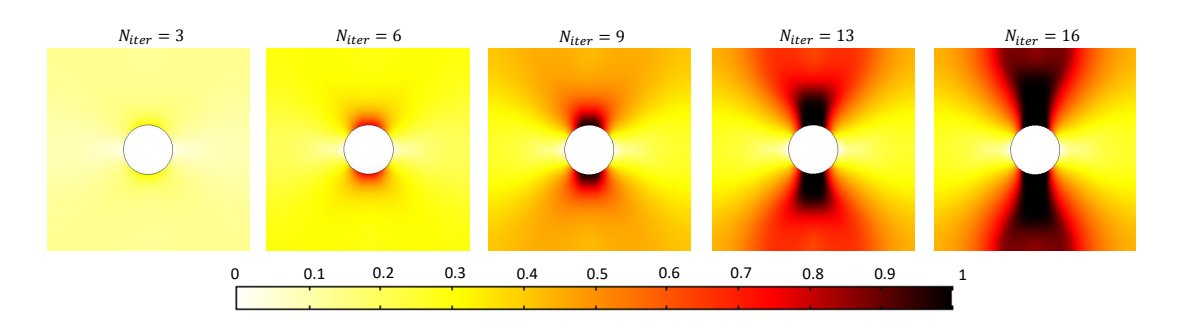


Figure 21: Non-homogeneous extension test. Contour plots of maximum  $D_{\eta}(\theta)$  over  $\theta \in [0, 2\pi]$  for increasing loading steps.

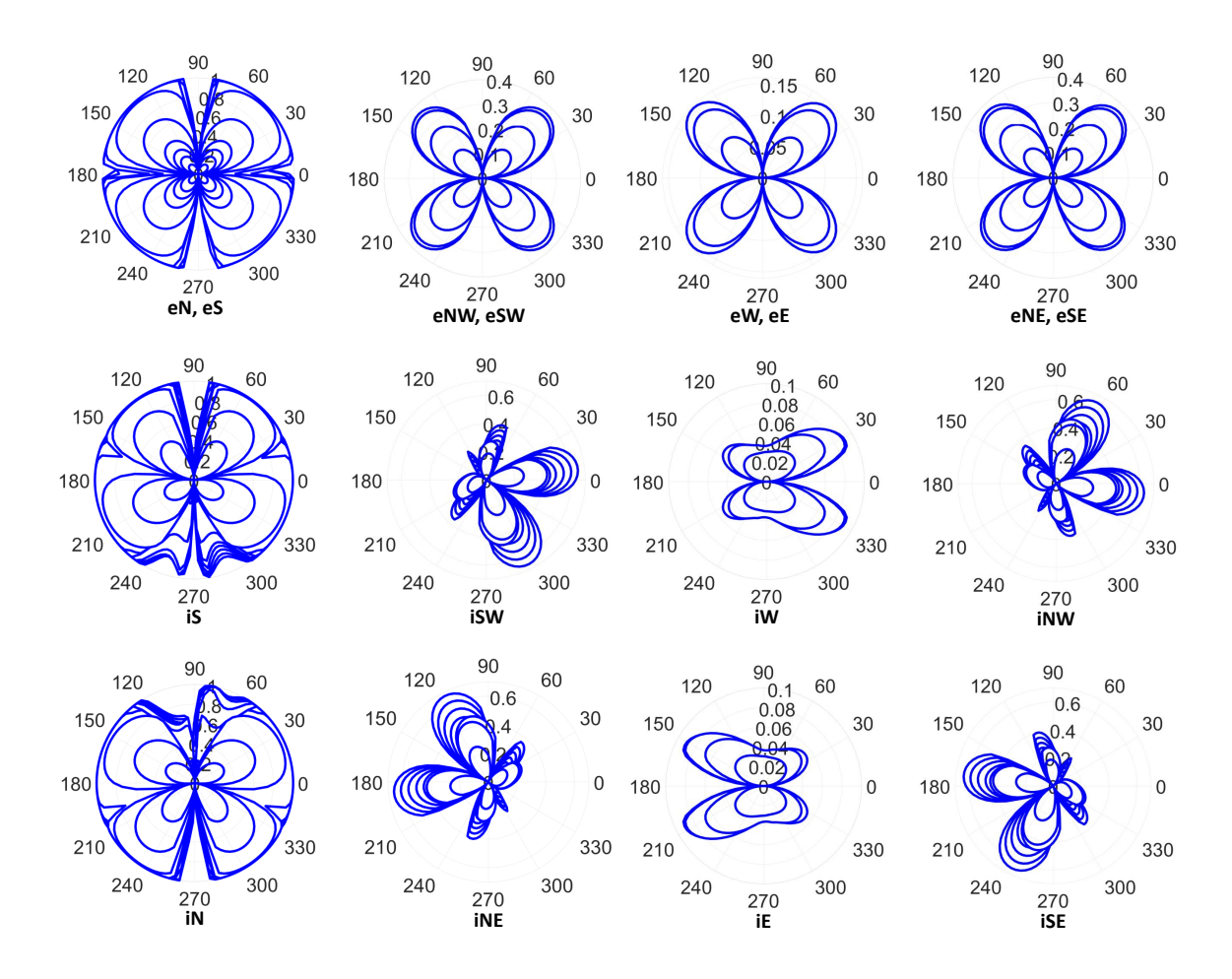


Figure 22: Non-homogeneous extension test. Evolution of  $D_{\tau}(\theta)$  at different points of the specimen (see the legend in Fig. 11).

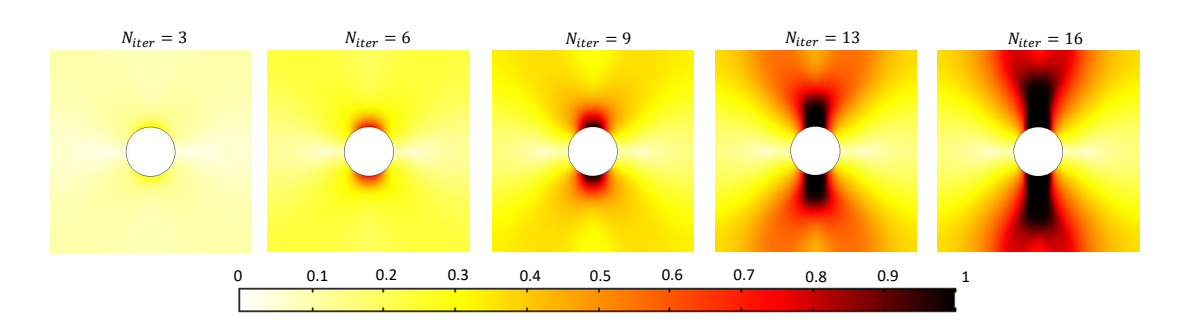


Figure 23: Non-homogeneous extension test. Contour plots of maximum  $D_{\tau}(\theta)$  over  $\theta \in [0, 2\pi]$  for increasing loading steps.

To further explicate the damage evolution and failure process, in Figs. 24, 25, and 26 we show the contour plots of elastic (top) and dissipated (bottom) energy densities for increasing loading steps for the three loading cases.

For the case of compression, both elastic and dissipated energy concentrates along the hole vertical diameter as expected classically. However, the dominant mechanism of damage is micro-shear as seen from contours of damage variables in Figs. 12 through 15, although dissipation in the vicinity of the hole is a complex combination of micro-crushing, micro-separation, and micro-shear for grain-pairs. The energy concentration in compression is in contrast to that for extension test (see Fig. 26), which

proceeds in a similar manner in early part of the loading eventually concentrating into a narrow zone. Indeed it is worthwhile to remark that a strain localization is occurring in the extension test, leading to a vertical brittle fracture. Considering that the study of brittle fracture in granular materials to be beyond the scope of the present paper, further investigations will be devoted in the future to analyze more thoroughly this fracture propagation.

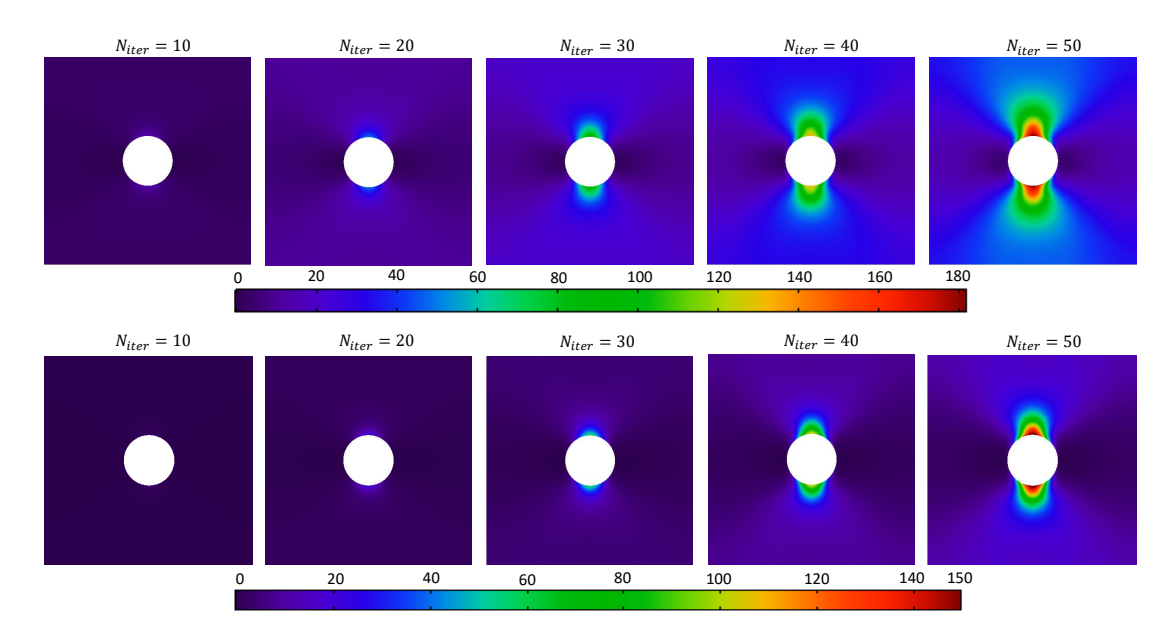


Figure 24: Non-homogeneous compression test. Contour plots of elastic (top) and dissipated (bottom) energy densities for increasing loading steps. All quantities are expressed in  $J/m^2$ .

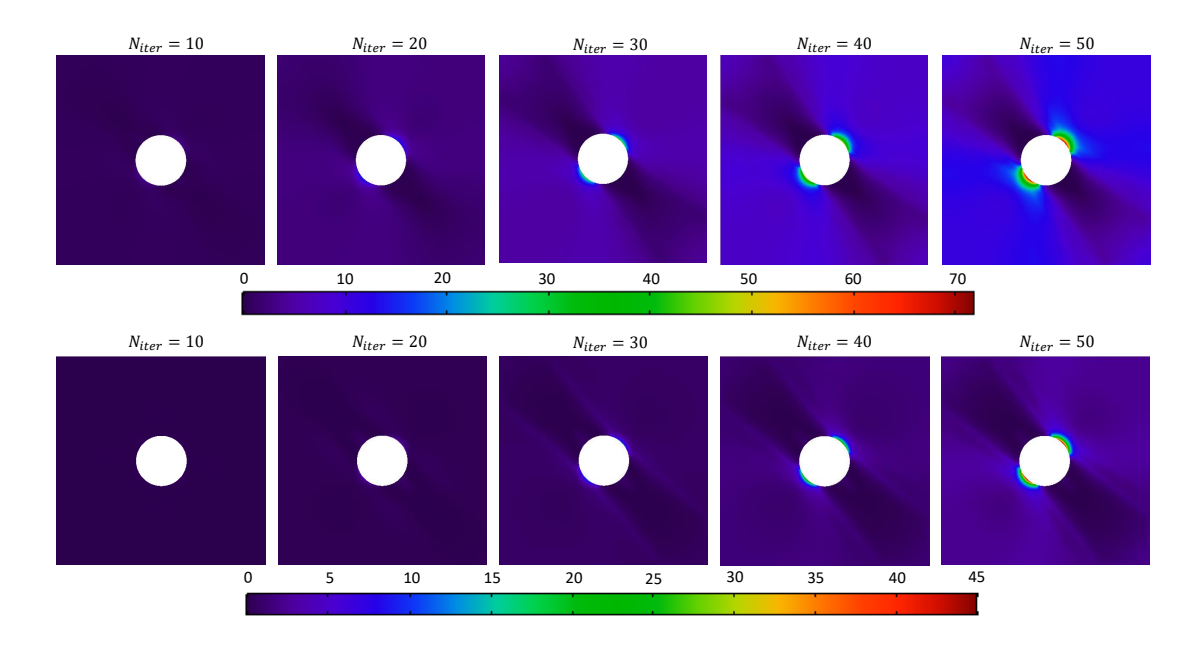


Figure 25: Non-homogeneous shearing test. Contour plots of elastic (top) and dissipated (bottom) energy densities for increasing loading steps. All quantities are expressed in  $J/m^2$ .

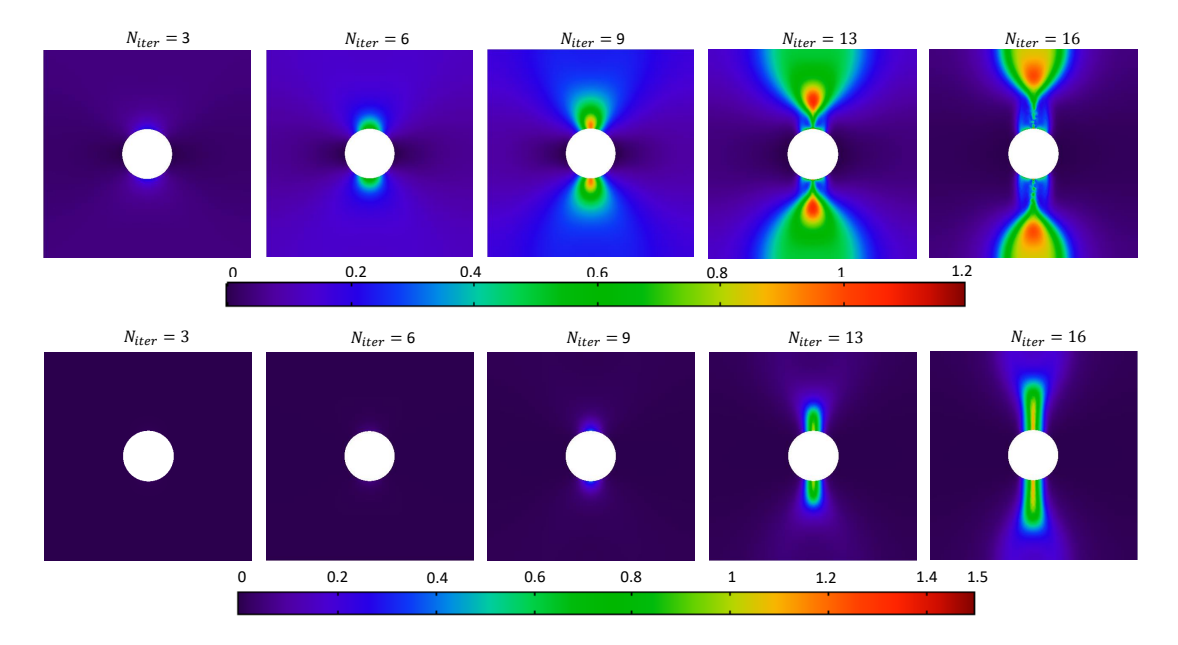


Figure 26: Non-homogeneous extension test. Contour plots of elastic (top) and dissipated (bottom) energy densities for increasing loading steps. All quantities are expressed in  $J/m^2$ .

# Concluding Remarks

The key contribution of this paper is the development of damage model for material with granular microstructures based upon purely mechanical concepts utilizing energy and variational approach. Further, by incorporating a granular micromechanics approach, a procedure is developed for linking the micro-scale (or grain-pair scale) to the continuum description. The following points highlight the main developments of the model derived in this work:

- Derivation of objective kinematic descriptors for grain-pair relative displacement in granular materials undergoing finite deformations.
- Derivation of the Karush-Kuhn-Tucker (KKT) type conditions for the grain-pair damage evolution and the Euler-Lagrange equations for evolution of grain-pair relative displacement as supplementary conditions based upon a novel non-standard variational principle (termed here as hemivariational).
- Implementation of grain-pair energy and dissipation functionals that exploit the tension-compression asymmetry as a unique feature of materials with granular microstructures.

The following points highlight the main findings of the presented work:

- Grain-pairs oriented in different directions experience different loading histories, and therefore, different damage evolution for the normal and tangent components of every grain-pair interaction leading to damage-induced anisotropic response of the continua.
- For non-homogeneous deformations, every material point of a continuum evolves in a different way.
- Due to the tension-compression asymmetric behavior of grain-pair and the influence of strain-gradients, erstwhile isotropic and non-chiral material transforms into anisotropic material with chirality.
- Strain gradients in the continuum model not only regularize the (elastic) results, but are necessary from a physical viewpoint to correctly describe the damage-induced evolution of the characteristic length scale as well as chirality and better characterization of anisotropy.

# Acknowledgments

 ${
m AM}$  is supported in part by the United States National Science Foundation grant CMMI -1727433.

#### References

- [1] B.E. Abali, W.H. Müller, and F. dell'Isola. Theory and computation of higher gradient elasticity theories based on action principles. *Archive of Applied Mechanics*, pages 1–16, 2017.
- [2] J-J. Alibert, A. Della Corte, I. Giorgio, and A. Battista. Extensional elastica in large deformation as\gamma-limit of a discrete 1d mechanical system. Zeitschrift f\u00fcr angewandte Mathematik und Physik, 68(2):42, 2017.
- [3] J-J. Alibert, P. Seppecher, and F. dell'Isola. Truss modular beams with deformation energy depending on higher displacement gradients. *Mathematics and Mechanics of Solids*, 8(1):51–73, 2003.
- [4] M. Ambati, T. Gerasimov, and L. De Lorenzis. Phase-field modeling of ductile fracture. *Computational Mechanics*, 55(5), 2015.
- [5] M. Ambati, T. Gerasimov, and L. Lorenzis. A review on phase-field models of brittle fracture and a new fast hybrid formulation. *Computational Mechanics*, 55(2), 2015.
- [6] H. Amor, J-J. Marigo, and C. Maurini. Regularized formulation of the variational brittle fracture with unilateral contact: numerical experiments. *Journal of the Mechanics and Physics of Solids*, 57(8):1209–1229, 2009.
- [7] U. Andreaus, F. dell'Isola, I. Giorgio, L. Placidi, T. Lekszycki, and N.L. Rizzi. Numerical simulations of classical problems in two-dimensional (non) linear second gradient elasticity. *International Journal of Engineering Science*, 108:34–50, 2016.
- [8] N. Auffray, J. Dirrenberger, and G. Rosi. A complete description of bi-dimensional anisotropic strain-gradient elasticity. *International Journal of Solids and Structures*, 69:195–206, 2015.
- [9] A. Battista, L. Rosa, R. dell'Erba, and L. Greco. Numerical investigation of a particle system compared with first and second gradient continua: Deformation and fracture phenomena. *Mathematics and Mechanics of Solids*, page 1081286516657889, 2016.
- [10] B. Bourdin, G. Francfort, and J-J. Marigo. Numerical experiments in revisited brittle fracture. Journal of the Mechanics and Physics of Solids, 48(4):797–826, 2000.
- [11] B. Bourdin, G. Francfort, and J-J. Marigo. The variational approach to fracture. *Journal of elasticity*, 91(1):5–148, 2008.
- [12] Ching S Chang and Jian Gao. Second-gradient constitutive theory for granular material with random packing structure. *International Journal of Solids and Structures*, 32(16):2279–2293, 1995.
- [13] B. Chiaia, O. Kumpyak, L. Placidi, and V. Maksimov. Experimental analysis and modeling of two-way reinforced concrete slabs over different kinds of yielding supports under short-term dynamic loading. *Engineering Structures*, 96:88–99, 2015.
- [14] L. Contrafatto, M. Cuomo, and F. Fazio. An enriched finite element for crack opening and rebar slip in reinforced concrete members. *International journal of fracture*, 178(1-2):33-50, 2012.
- [15] L. Contrafatto, M. Cuomo, and L. Greco. Meso-scale simulation of concrete multiaxial behaviour. European Journal of Environmental and Civil Engineering, pages 1–16, 2016.
- [16] M. Cuomo, F. dell'Isola, and L. Greco. Simplified analysis of a generalized bias test for fabrics with two families of inextensible fibres. Zeitschrift f\u00fcr angewandte Mathematik und Physik, 67(3):1-23, 2016.
- [17] M. Cuomo, F. dell'Isola, L. Greco, and N.L. Rizzi. First versus second gradient energies for planar sheets with two families of inextensible fibres: Investigation on deformation boundary layers, discontinuities and geometrical instabilities. *Composites Part B: Engineering*, 2016.
- [18] F. D'Annibale, G. Rosi, and A. Luongo. Linear stability of piezoelectric-controlled discrete mechanical systems under nonconservative positional forces. *Meccanica*, 50(3):825–839, 2015.

- [19] G. Del Piero, G. Lancioni, and R. March. A variational model for fracture mechanics: numerical experiments. *Journal of the Mechanics and Physics of Solids*, 55(12):2513–2537, 2007.
- [20] F. dell'Isola, A. Della Corte, I. Giorgio, and D. Scerrato. Pantographic 2d sheets: Discussion of some numerical investigations and potential applications. *International Journal of Non-Linear Mechanics*, 80:200–208, 2016.
- [21] F. dell'Isola, I. Giorgio, and U. Andreaus. Elastic pantographic 2d lattices: a numerical analysis on static response and wave propagation. In *Proceedings of the Estonian Academy of Sciences*, volume 64, pages 219–225, 2015.
- [22] F. dell'Isola, I. Giorgio, M. Pawlikowski, and N. Rizzi. Large deformations of planar extensible beams and pantographic lattices: heuristic homogenization, experimental and numerical examples of equilibrium. *Proc. R. Soc. A*, 472(2185):20150790, 2016.
- [23] F. dell'Isola, T. Lekszycki, M. Pawlikowski, R. Grygoruk, and L. Greco. Designing a light fabric metamaterial being highly macroscopically tough under directional extension: first experimental evidence. Zeitschrift für angewandte Mathematik und Physik, 66:3473–3498, 2015.
- [24] F. dell'Isola, A. Madeo, and P. Seppecher. Boundary conditions at fluid-permeable interfaces in porous media: A variational approach. *International Journal of Solids and Structures*, 46(17):3150–3164, 2009.
- [25] V. A Eremeyev, F. dell'Isola, C. Boutin, and D. Steigmann. Linear pantographic sheets: existence and uniqueness of weak solutions. 2017.
- [26] G. Francfort and J-J. Marigo. Revisiting brittle fracture as an energy minimization problem. Journal of the Mechanics and Physics of Solids, 46(8):1319–1342, 1998.
- [27] F. Freddi and G. Royer-Carfagni. Variational fracture mechanics to model compressive splitting of masonry-like materials. *Annals of Solid and Structural Mechanics*, 2(2):57–67, 2011.
- [28] G. Ganzosch, F. dell'Isola, e. Turco, T. Lekszycki, and W.H. Müller. Shearing tests applied to pantographic structures. *Acta Polytechnica CTU Proceedings*, 7:1–6, 2016.
- [29] I. Giorgio, A. Della Corte, F. dell'Isola, and D. Steigmann. Buckling modes in pantographic lattices. *Comptes rendus Mecanique*, 2016.
- [30] Ivan Giorgio, Michele De Angelo, Emilio Turco, and Anil Misra. A biot-cosserat two-dimensional elastic nonlinear model for a micromorphic medium. *Continuum Mechanics and Thermodynamics*, pages 1–13, 2019.
- [31] Ivan Giorgio, Francesco dell'Isola, and Anil Misra. Chirality in 2d cosserat media related to stretch-micro-rotation coupling with links to granular micromechanics. *International Journal of Solids and Structures*, 2020.
- [32] P. Harrison, D. Anderson, M.F. Alvarez, E. Bali, and Y. Mateos. Measuring and modelling the inplane bending stiffness and wrinkling behaviour of engineering fabrics. *EUROMECH Colloquium* 569: Multiscale Modeling of Fibrous and Textile Materials, Chatenay-Malabry, 2016.
- [33] G. Lancioni. Numerical results from different variational theories of fracture. In Giornata IGF Forni di Sopra (UD) 2010.
- [34] G. Lancioni and G. Royer-Carfagni. The variational approach to fracture mechanics. a practical application to the french panthéon in paris. *Journal of elasticity*, 95(1):1–30, 2009.
- [35] T. Li, J-J. Marigo, D. Guilbaud, and S. Potapov. Gradient damage modeling of brittle fracture in an explicit dynamics context. *International Journal for Numerical Methods in Engineering*, 108(11):1381–1405, 2016.
- [36] T.Y. Li, J-J. Marigo, D. Guilbaud, and S. Potapov. Variational approach to dynamic brittle fracture via gradient damage models. In *Applied mechanics and materials*, volume 784, pages 334–341. Trans Tech Publ, 2015.
- [37] J-J. Marigo, C. Maurini, and K. Pham. An overview of the modelling of fracture by gradient damage models. *Meccanica*, 2016.

- [38] C. Miehe, M. Hofacker, and F. Welschinger. A phase field model for rate-independent crack propagation: Robust algorithmic implementation based on operator splits. *Computer Methods in Applied Mechanics and Engineering*, 199(45):2765–2778, 2010.
- [39] A. Misra. Effect of asperity damage on shear behavior of single fracture. Engineering Fracture Mechanics, 69(17):1997–2014, 2002.
- [40] A. Misra and P. Poorsolhjouy. Granular micromechanics model for damage and plasticity of cementitious materials based upon thermomechanics. *Mathematics and Mechanics of Solids*, page 1081286515576821, 2015.
- [41] A. Misra and V. Singh. Micromechanical model for viscoelastic materials undergoing damage. Continuum Mechanics and Thermodynamics, pages 1–16, 2013.
- [42] A.l Misra and V. Singh. Thermomechanics-based nonlinear rate-dependent coupled damage-plasticity granular micromechanics model. *Continuum Mechanics and Thermodynamics*, 27(4-5):787, 2015.
- [43] Anil Misra, Placidi Luca, and Emilio Turco. Variational methods for discrete models of granular materials. Encylopedia of continuum mechanics. Berlin: Springer-Verlag. Heidelberg, ISBN: 978-3-662-53605-6, doi: 10.1007/978-3-662-53605-6, 2020.
- [44] Anil Misra, Nima Nejadsadeghi, Michele De Angelo, and Luca Placidi. Chiral metamaterial predicted by granular micromechanics: verified with 1d example synthesized using additive manufacturing. Continuum Mechanics and Thermodynamics, pages 1–17, 2020.
- [45] Kevin M Moerman, Ciaran K Simms, and Thomas Nagel. Control of tension—compression asymmetry in ogden hyperelasticity with application to soft tissue modelling. *Journal of the mechanical behavior of biomedical materials*, 56:218–228, 2016.
- [46] Komi Espoir Násouglo, José A Rodríguez-Martínez, A Vaz-Romero, and Oana Cazacu. The combined effect of plastic orthotropy and tension-compression asymmetry on the development of necking instabilities in flat tensile specimens subjected to dynamic loading. *International Journal of Solids and Structures*, 159:272–288, 2019.
- [47] Nima Nejadsadeghi and Anil Misra. Extended granular micromechanics approach: a micromorphic theory of degree n. *Mathematics and Mechanics of Solids*, 25(2):407–429, 2020.
- [48] Tomasz Ozyhar, Stefan Hering, and Peter Niemz. Viscoelastic characterization of wood: Time dependence of the orthotropic compliance in tension and compression. *Journal of Rheology*, 57(2):699–717, 2013.
- [49] K. Pham, H. Amor, J-J. Marigo, and C. Maurini. Gradient damage models and their use to approximate brittle fracture. *International Journal of Damage Mechanics*, 20(4):618–652, 2011.
- [50] L. Placidi. A variational approach for a nonlinear 1-dimensional second gradient continuum damage model. *Continuum Mechanics and Thermodynamics*, 27(4-5):623, 2015.
- [51] Luca Placidi. A variational approach for a nonlinear one-dimensional damage-elasto-plastic second-gradient continuum model. *Continuum Mechanics and Thermodynamics*, 28(1-2):119–137, 2016.
- [52] Luca Placidi and Emilio Barchiesi. Energy approach to brittle fracture in strain-gradient modelling. Proceedings of the Royal Society A: Mathematical, Physical and Engineering Sciences, 474(2210):20170878, 2018.
- [53] Luca Placidi, Emilio Barchiesi, and Anil Misra. A strain gradient variational approach to damage: a comparison with damage gradient models and numerical results. *Mathematics and Mechanics of Complex Systems*, 6(2):77–100, 2018.
- [54] Luca Placidi, Anil Misra, and Emilio Barchiesi. Two-dimensional strain gradient damage modeling: a variational approach. Zeitschrift für angewandte Mathematik und Physik, 69(3):56, 2018.
- [55] Luca Placidi, Anil Misra, and Emilio Barchiesi. Simulation results for damage with evolving microstructure and growing strain gradient moduli. *Continuum Mechanics and Thermodynamics*, 31(4):1143–1163, 2019.

- [56] Payam Poorsolhjouy and Anil Misra. Effect of intermediate principal stress and loading-path on failure of cementitious materials using granular micromechanics. *International Journal of Solids and Structures*, 108:139–152, 2017.
- [57] Payam Poorsolhjouy and Anil Misra. Granular micromechanics based continuum model for grain rotations and grain rotation waves. *Journal of the Mechanics and Physics of Solids*, 129:244–260, 2019.
- [58] D. Scerrato, I. Giorgio, A. Della Corte, A. Madeo, N. Dowling, and F. Darve. Towards the design of an enriched concrete with enhanced dissipation performances. *Cement and Concrete Research*, 84:48–61, 2016.
- [59] D. Scerrato, I. Giorgio, A. Della Corte, A. Madeo, and A. Limam. A micro-structural model for dissipation phenomena in the concrete. *International Journal for Numerical and Analytical Methods in Geomechanics*, 2015.
- [60] G. Sciarra, F. dell'Isola, and O. Coussy. Second gradient poromechanics. *International Journal of Solids and Structures*, 44(20):6607–6629, 2007.
- [61] P. Seppecher, J.-J. Alibert, and F. dell'Isola. Linear elastic trusses leading to continua with exotic mechanical interactions. In *Journal of Physics: Conference Series*, volume 319, page 012018. IOP Publishing, 2011.
- [62] P. Sicsic and J-J. Marigo. From gradient damage laws to griffith's theory of crack propagation. Journal of Elasticity, pages 1–20, 2013.
- [63] M. Spagnuolo, K. Barcz, A. Pfaff, F. dell'Isola, and P. Franciosi. Qualitative pivot damage analysis in aluminum printed pantographic sheets: numerics and experiments. *Mechanics Research Communications*, 2017.
- [64] D.J. Steigmann and F. dell'Isola. Mechanical response of fabric sheets to three-dimensional bending, twisting, and stretching. *Acta Mechanica Sinica*, 31(3):373–382, 2015.
- [65] Nicolas Triantafyllidis and S Bardenhagen. On higher order gradient continuum theories in 1-d nonlinear elasticity, derivation from and comparison to the corresponding discrete models. *Journal of Elasticity*, 33(3):259–293, 1993.
- [66] E. Turco, F. dell'Isola, A. Cazzani, and N.L. Rizzi. Hencky-type discrete model for pantographic structures: numerical comparison with second gradient continuum models. Zeitschrift für angewandte Mathematik und Physik, 67, 2016.
- [67] E. Turco, F. dell'Isola, N.L. Rizzi, R. Grygoruk, W.H. Müller, and C. Liebold. Fiber rupture in sheared planar pantographic sheets: Numerical and experimental evidence. *Mechanics Research Communications*, 76:86–90, 2016.
- [68] E. Turco, M. Golaszewski, A. Cazzani, and N.L. Rizzi. Large deformations induced in planar pantographic sheets by loads applied on fibers: experimental validation of a discrete lagrangian model. *Mechanics Research Communications*, 76:51–56, 2016.
- [69] E. Turco, M. Golaszewski, I. Giorgio, and F. D'Annibale. Pantographic lattices with non-orthogonal fibres: Experiments and their numerical simulations. Composites Part B: Engineering, 118:1–14, 2017.
- [70] C. Wang and X. Qian. Heaviside projection based aggregation in stress constrained topology optimization. *International Journal for Numerical Methods in Engineering*, 115(7):849–871, 2018.
- [71] Y. Yang and A. Misra. Micromechanics based second gradient continuum theory for shear band modeling in cohesive granular materials following damage elasticity. *International Journal of Solids and Structures*, 49(18):2500–2514, 2012.